JEM Journal of Experimental Medicine

ARTICLE

The lifespan and kinetics of human dendritic cell subsets and their precursors in health and inflammation

Ruth Lubin[1*], Amit A. Patel[2*], Jonas Mackerodt[3*], Yan Zhang[4], Rotem Gvili[1], Kevin Mulder[5,6,7], Charles-Antoine Dutertre[5,6], Parinaaz Jalali[2], James R.W. Glanville[2], Idit Hazan[1], Nikhila Sridharan[1], Gurion Rivkin[8], Ayse Akarca[9], Teresa Marafioti[9], Derek W. Gilroy[2], Leonid Kandel[8], Alexander Mildner[10,11], Asaf Wilensky[12], Becca Asquith[3], Florent Ginhoux[5,13,14,15], Derek Macallan[4,16], and Simon Yona[1]

Dendritic cells (DC) are specialized mononuclear phagocytes that link innate and adaptive immunity. They comprise two principal subsets: plasmacytoid DC (pDC) and conventional DC (cDC). Understanding the generation, differentiation, and migration of cDC is critical for immune homeostasis. Through human in vivo deuterium-glucose labeling, we observed the rapid appearance of AXL$^+$ Siglec6$^+$ DC (ASDC) in the bloodstream. ASDC circulate for ∼2.16 days, while cDC1 and DC2 circulate for ∼1.32 and ∼2.20 days, respectively, upon release from the bone marrow. Interestingly, DC3, a cDC subset that shares several similarities with monocytes, exhibits a labeling profile closely resembling that of DC2. In a human in vivo model of cutaneous inflammation, ASDC were recruited to the inflammatory site, displaying a distinctive effector signature. Taken together, these results quantify the ephemeral circulating lifespan of human cDC and propose functions of cDC and their precursors that are rapidly recruited to sites of inflammation.

Introduction

Dendritic cells (DC) act as a critical bridge between the innate sensing of pathogens and the orchestration of adaptive immunity (Nussenzweig and Steinman, 1980). The ability of DC to mount an adaptive immune response toward an array of pathogens as well as provide self-tolerance is attributed—in part—to the diversity of the DC family. Under healthy homeostasis, DC comprise two distinct lineages: plasmacytoid DC (pDC), renowned for their capacity to produce type 1 interferons in response to viral infections, and conventional DC (cDC). The cDC lineage efficiently activates naïve T cells (Tussiwand et al., 2023).

Originally, human cDC were categorized into two groups: cDC1 (CD141$^+$) and cDC2 (CD1c$^+$) (Guilliams et al., 2014). Single-cell transcriptomics and high-dimensional protein analysis unveiled additional diversity within the cDC family. The CD1c$^+$ population can be split into DC2 and DC3 (Kvedaraite and Ginhoux, 2022). DC3 are understood to have a distinct ontogeny exhibiting several similarities to classical monocytes (Villani et al., 2017; Dutertre et al., 2019; Bourdely et al., 2020; Cytlak et al., 2020). Another member of the DC family is the circulating AXL$^+$ Siglec-6$^+$ DC (ASDC), also designated pre-DC, transitional DC (tDC), or DC5 (Leylek et al., 2019; See et al., 2017; Villani et al., 2017). Finally, a migratory immune regulatory DC (mregDC) "state" has been coined to describe a distinct molecular status within the cDC family (Ginhoux et al., 2022).

It remained controversial if, or when, the DC and monocyte lineages diverge during hematopoiesis. A breakthrough in solving this puzzle arose with the discovery of the common DC

[1]The Institute of Biomedical and Oral Research, Faculty of Dental Medicine, Hebrew University, Jerusalem, Israel; [2]Division of Medicine, University College London, London, UK; [3]Department of Infectious Disease, Imperial College London, London, UK; [4]Institute for Infection and Immunity, St. George's, University of London, London, UK; [5]Gustave Roussy Cancer Campus, Villejuif, France; [6]Institut National de la Santé Et de la Recherche Médicale (INSERM) U1015, Equipe Labellisée—Ligue Nationale Contre le Cancer, Villejuif, France; [7]Université Paris-Saclay, Gif-sur-Yvette, France; [8]Department of Orthopaedic Surgery, Hadassah-Hebrew University Medical Center, Jerusalem, Israel; [9]University College London, London, UK; [10]MediCity Research Laboratory, University of Turku, Turku, Finland; [11]InFLAMES Research Flagship, University of Turku, Turku, Finland; [12]Department of Periodontology, Faculty of Dental Medicine, Hadassah Medical Center, Hebrew University of Jerusalem, Jerusalem, Israel; [13]Singapore Immunology Network, Agency for Science, Technology and Research, Singapore; [14]Department of Immunology and Microbiology, Shanghai Institute of Immunology, Shanghai Jiao Tong, University School of Medicine, Shanghai, China; [15]Translational Immunology Institute, SingHealth Duke-NUS Academic Medical Centre, Singapore; [16]St. George's University Hospitals NHS Foundation Trust, London, UK.

*R. Lubin, A.A. Patel, and J. Mackerodt contributed equally to this paper. Correspondence to Simon Yona: s.yona@mail.huji.ac.il.

progenitor (CDP, murine/hCDP, human), a cell type that gives rise exclusively to DC (Lee et al., 2015; Liu et al., 2009; Onai et al., 2007), downstream of the monocyte–DC progenitor (MDP) (Fogg et al., 2006; Lee et al., 2015). An intermediate cell type between the CDP and cDC, the pre-cDC/hpre-cDC, has since been identified (Breton et al., 2015; Ginhoux et al., 2009; Liu et al., 2009; Schlitzer et al., 2015; Schraml et al., 2013). These murine pre-cDC exit the bone marrow and migrate to peripheral tissues, where they divide and differentiate into cDC, which themselves have residual proliferative capacity (Cabeza-Cabrerizo et al., 2019; Diao et al., 2004; Ginhoux et al., 2009; Liu et al., 2007; Naik et al., 2006, 2007). The murine Ly6C$^+$ MDP gives rise to a pro-DC3 that develops into DC3 (Liu et al., 2023), while the precise origin of the human DC3 remains to be fully resolved. Conversely, pDC may mature within the bone marrow via a pre-pDC route, at least in mice (Jackson et al., 2011; Onai et al., 2007; Toyama-Sorimachi et al., 2005).

Translating such ontogenetic models to human biology remains challenging. In rodents, the DC lineage appears predestined at an early stage of development (Grajales-Reyes et al., 2015; Schlitzer et al., 2015), yet the fate and lifespan of human cDC subsets during healthy homeostasis remains unclear. Human ASDC (See et al., 2017; Villani et al., 2017) and cDC coexist in peripheral circulation, but the relationship of these cells is only now being examined (See et al., 2017; Sulczewski et al., 2023; Villani et al., 2017). Added to this are the complexities that arise during inflammation. Inflammation induces sequential events including emergency hematopoiesis and cell migration, which impact mononuclear phagocyte populations in ways that fall outside the rules governing healthy homeostasis (Guilliams et al., 2018; Patel et al., 2017).

The human body maintains a consistent number of cDC by means of cell proliferation, differentiation, survival, and cell death under healthy physiological conditions (Patel et al., 2021). During inflammation, this finely tuned system must adapt to produce sufficient leucocytes to combat injury or infection and replace those dysregulated by the inflammatory challenge. Understanding this response may present a potential therapeutic opportunity. A key advance in examining human leucocyte kinetics in vivo arose with the advent of non-toxic stable isotope labeling methods (Busch et al., 2007; Macallan et al., 2009). Specifically, using deuterium-labeled glucose or water it is possible to quantify rates of cell division in dividing cell populations (Patel et al., 2017). The deuterium-labeled glucose approach is particularly suited to study rapidly dividing cells and has been applied in humans to study the turnover of T cell populations such as regulatory T cells (Vukmanovic-Stejic et al., 2006), memory T cell subsets in HIV infection (Zhang et al., 2013), and, more recently, cells of the innate immune system, including neutrophils (Lahoz-Beneytez et al., 2016) and monocytes (Patel et al., 2017; Tak et al., 2017).

Here, we used an in vivo deuterium-glucose–labeled approach to investigate the fate and lifespan of cDC populations and their precursors in healthy human volunteers. Our data estimate the mean circulating lifespan of cDC1, DC2, DC3, and ASDC and support a model in which DC2 arise from ASDC in the bone marrow and blood. Remarkably, the cDC family showed striking similarities in their circulating kinetics in vivo, including DC3 that most likely arise from a distinct progenitor (Cytlak et al., 2020). Next, we examined the impact of local inflammation on tissue DC subpopulations using a human model of bacterial-induced dermal inflammation. Finally, we assessed the DC subsets with single-cell transcriptome analysis and constructed a comprehensive map of how human DC subsets alter from steady state to inflammation.

Results

Characterization of human DC subsets and their precursors

To investigate human cDC kinetics under steady state, we first sought to clearly define these cells in circulation by spectral flow cytometry. Our strategy for DC classification considered developments in the identification of human DC subsets (Dutertre et al., 2019; See et al., 2017; Villani et al., 2017). In view of the challenges in forming a clear consensus for each DC population, we incorporated several markers for ASDC, cDC1, DC2, DC3, and pDC and developed a global strategy to identify these five populations (Fig. S1 a). To this end, we characterized the DC subsets in the circulation using a principal panel and then confirmed their classification with additional markers. DC were defined as LIN$^-$ HLA-DR$^+$ cells, with ASDC and pDC being CD123$^+$ and CD45RA$^+$; ASDC were discriminated from pDC as Siglec-6$^+$ AXL$^+$ CD5$^+$ (Fig. 1 a and Fig. S1 a). pDC on the other hand showed higher expression of CD303 (Fig. 1 a). Curiously, we occasionally noticed an unidentified population within the global DC gate, which was defined as HLA-DR$^+$ LIN$^-$ CD45RA$^-$ CD123$^+$ cells. Further analysis established this population to be CD203c$^+$ and consequently belong to basophils (Fig. S1 b). cDC were defined as CD123$^-$ CD11c$^+$ and could be further segregated into CD141$^+$ CD33$^+$ CLEC9a$^+$ cDC1, while cDC2 were defined as CD1c$^+$ CD33$^+$ FceR1a$^+$and CX$_3$CR1$^+$ cells (Fig. 1 a and Fig. S1 a). The cDC2 population was further divided into CD5$^+$ DC2 and CD5$^-$ DC3 (Cossarizza et al., 2021; Dutertre et al., 2019), and this DC3 population expressed varying levels of CD14 (Fig. 1 a and Fig. S1 a). The morphology of these DC populations was confirmed by cell sorting and subsequent cytospin. A clear distinction between pDCs and other DC populations was evident, with pDCs exhibiting their distinctive plasma cell–like morphology (Fig. 1 b). Taken together, these findings established a straightforward accessible regime to identify human DC subsets by combining several previously described strategies.

Next, absolute numbers of blood DC subsets were calculated using volumetric flow cytometry analysis. Circulating DC compose ∼0.5% of all circulating CD45$^+$ leucocytes in healthy individuals. pDC are the most abundant of these populations (Fig. 1 c). Within the cDC population of cells, cDC1 circulate at less than a tenth of the concentration of DC2 and DC3 population combined. While ASDC account for ∼2% of all blood DC (Fig. 1 c). Quantification was also performed for the bone marrow DC subsets using a similar staining strategy but with the additional exclusion of CD34$^+$ cells (Fig. S1 c, quantification Fig. 1 d) (Cytlak et al., 2020). Finally, the percentage and total blood and bone marrow DC numbers were calculated (Fig. S1 d). The remainder

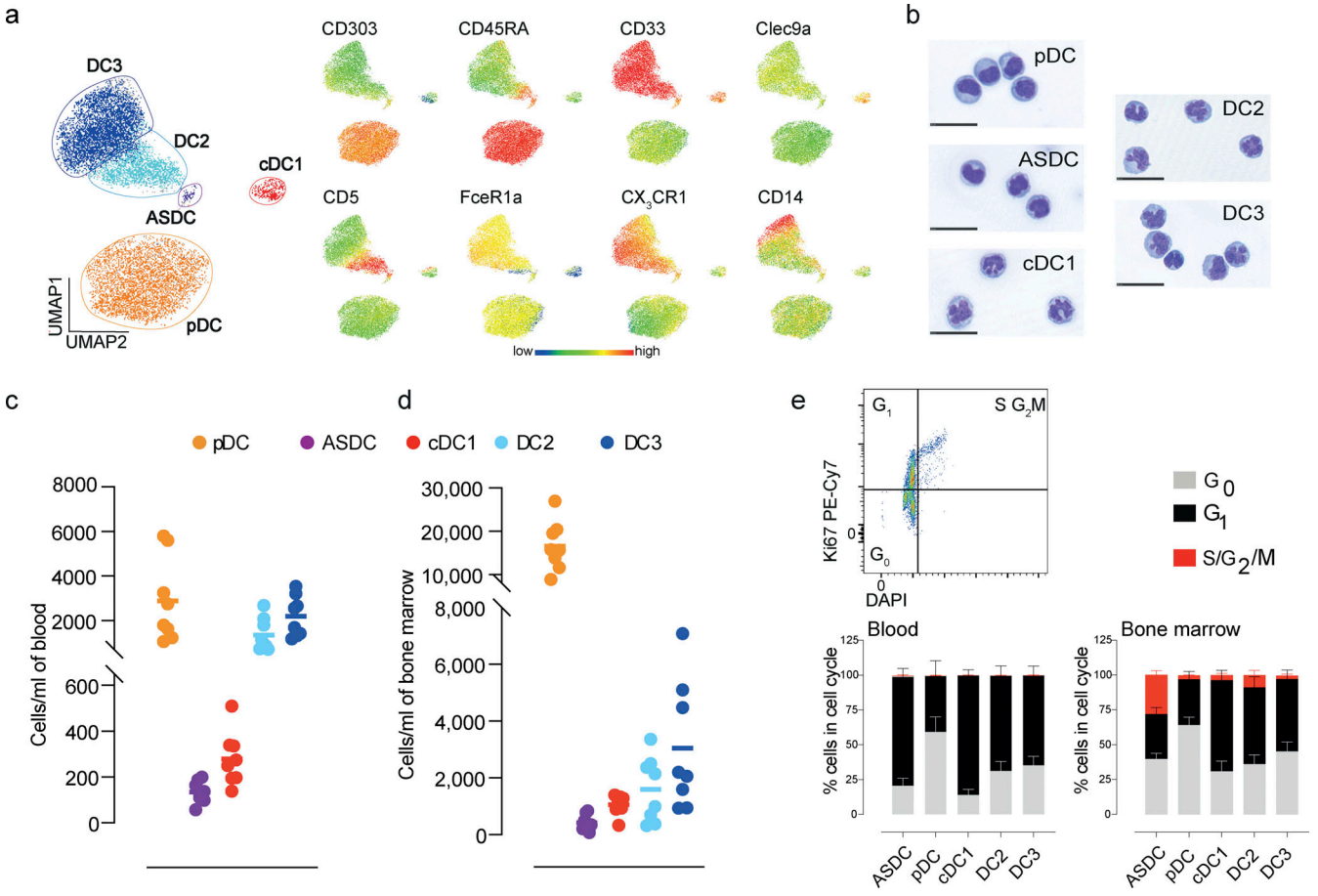

Figure 1. **Characterization of circulating human DC subsets.** Peripheral blood DC subsets were analyzed by spectral flow cytometry. **(a)** UMAP of each DC subset defined in Fig. S1 a, illustrating several discriminating membrane markers that can be used to further identify each population for example Clec9a for cDC1 or CD33 for cDC populations. The flow cytometry analysis is representative of 15 healthy volunteers. **(b)** Representative cytospin images stained with methylene blue and eosin, scale bar 25 µm. **(c and d)** Quantification of DC subsets in healthy (c) peripheral blood and (d) bone marrow from eight individuals. **(e)** A representative plot illustrating DC subset analysis investigating DNA content and Ki67 expression as indicators of the cell cycle. The percentage of cells in G_0, G_1, or S G_2 M phases of cell cycle in peripheral human blood or bone marrow from five individuals. (Error bars correspond to ± SEM.)

of this study will concentrate on the human cDC lineage. To assess the proliferation status of each cDC subset, we examined their cell cycle state in fresh blood and bone marrow by employing Ki67 and DAPI staining, enabling the discrimination between cell cycle phases G_0, G_1 and S+G_2M. Murine pre-DC are understood to proliferate in the bone marrow or within tissues (Cabeza-Cabrerizo et al., 2019). As expected, the majority of blood DC examined were in G_0 or G_1 phase and not actively dividing (Fig. 1 e). In the bone marrow, very few adult cDC appeared to be actively proliferating. By contrast, around a third of ASDC were in the S+G_2M phases (Fig. 1 e), consistent with a proliferative population. According to these data, the approximate daily mean proliferation rate in the bone marrow was estimated for each population as cDC1 0.2, DC2 0.26, DC3 0.07, and ASDC 0.66 times per day (Fig. S1 e). This snapshot of cell cycle analysis laid the foundations for the proliferation characterization of each DC population within these settings but was unable to delineate the precise cellular kinetics and lifespan of these populations based on cell cycle phase length previously determined in T cells (Dowling et al., 2014).

Lifespan of circulating human cDC subsets in steady state

To investigate the lifespan and relationship of blood cDC subsets during healthy homeostasis, a 3-h pulse of deuterium-labeled glucose (6,6-$^2H_2$-glucose) was administered to healthy volunteers, and cDC subsets at sequential time points were analyzed thereafter for non-exchangeable DNA deuterium incorporation in dividing cells (Fig. 2 a), as previously described (Patel et al., 2017). Deuterium rapidly appeared in the plasma, reaching a plateau that persisted until the end of the dosing period and declined to baseline levels ∼6 h after the initial dose (Fig. S2 a). In this setting, time-dependent DNA deuterium-labeling levels in circulating cells reflect three rates: (i) the rate of cell division of the cells analyzed or their precursors; (ii) the rate of entry of labeled cells into the sampled compartment—in this case, the circulation; (iii) the rate of death or disappearance of labeled cells from the circulation. Analysis of the deuterium incorporation by gas chromatography–mass spectrometry (GC-MS) revealed that each cDC subset exhibited a highly consistent pattern in all volunteers (Fig. 2 b). DNA labeling curves were generated and then modeled to determine the lifespan of each circulating cDC subset. Deuterium incorporation was observed to be rapid

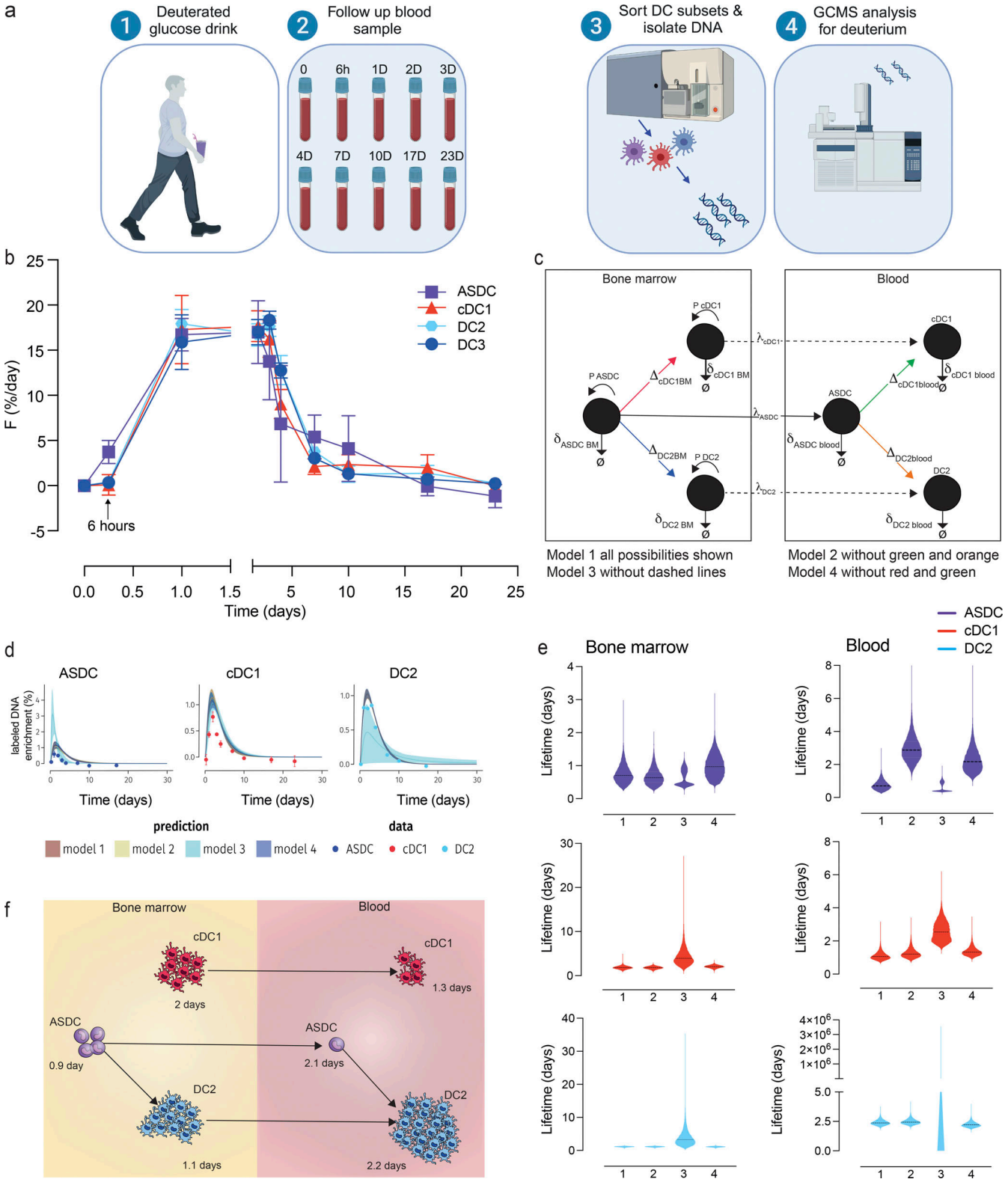

Figure 2. **In vivo labeling and a mathematical approach of modeling human DC subset kinetics. (a)** Protocol of in vivo labeling for the identification of newly divided cells. **(1)** Healthy volunteers received 20 g of deuterium-labeled glucose over 3 h. **(2 and 3)** DC subsets were subsequently sorted from whole blood over a 23-day (D) period; DNA was extracted to quantify the deuterium enrichment in each DC population by **(4)** GC-MS. **(b)** Fraction (F) of newly divided cells in peripheral blood ASDC, cDC1, DC2, and DC3 at time points following oral deuterium glucose in healthy volunteers; values were derived by dividing the DNA enrichment by the glucose deuterium area under the curve and expressed as %/day, shown as a mean ± SEM (n = 3–9 individuals per group). **(c)** Potential models examined for the calculation of circulating DC kinetics. Schematic depicts several plausible scenarios where ASDC develop into either DC2 and/or cDC1. P = proliferation, δ = death/disappearance, and λ = movement into the peripheral circulation. **(d)** The predictions of each model were summarized in terms of

the mean (solid line) and the standard deviation (shaded area) by solving the respective model using samples from their posterior distribution. The fitted data (dots) are superimposed onto the posterior predictions. These data are representative of one study participant. **(e)** Lifespan times of ASDC, cDC1, and DC2 in both the bone marrow and blood across each model. **(f)** Cartoon depicting the most probable model and lifespan of each DC subset.

as early as 1 day after labeling in circulating cDC1, DC2, and DC3 populations (Fig. 2 b). Labeled cDC1, DC2, and DC3 continued to accumulate in the bloodstream before starting to disappear from day 3 onwards, likely by migration into peripheral tissues—although cell death in the circulation might also explain the observed loss of labeled cells. Strikingly, the ASDC population appeared in the circulation as early as 6 h after the deuterium pulse, suggesting either a very short postmitotic dwell time prior to entering the circulation, or, alternatively, that cell division occurs within the circulating compartment; the latter scenario is unlikely given the cell cycle data in Fig. 1 e. These ASDC then followed a similar kinetic trajectory to the other cDC subsets.

To interpret these data (Fig. 2 b), we developed four models of cDC lineage topology in which cells undergo cell division and acquire label exclusively in the bone marrow before being released into the peripheral circulation (see Materials and methods; Fig. 2 c and Fig. S2 b) based on the prevailing hypotheses regarding cDC differentiation hierarchy. DC3 has been shown to have a distinct lineage and therefore was modeled separately. Model 1 is based on the hypothesis that ASDC may give rise to cDC1 and DC2 in both the bone marrow and blood (See et al., 2017). While others observed ASDC tend to aquire CD1c in culture (Villani et al., 2017). More recently, Sulczewski et al. (2023), demonstrated the ASDC potential to develop into DC2, which is the basis of model 4 where ASDC are assumed to be the precursor to DC2 while independent from cDC1. Nevertheless, additional hypothetical transitions were also explored in an unbiased fashion lacking either the release of cDC1 and DC2 into blood or differentiation in the blood (Fig. 2 c and Fig. S2 b, for a detailed explanation). Next, Bayesian inference was performed for all models to estimate the posterior parameter distributions. The goodness-of-fit for each model was quantified by the expected log pointwise predictive density (elpd), which was calculated using Pareto-smoothed importance sampling leave-one-out cross-validation (PSIS-LOO-CV) (Vehtari et al., 2017) (Fig. 2, d and e; and Fig. S2, c–g). Several models offered good fits to these data with minimal difference (models 1, 2, and 4; max[Δ elpd] = 0.1.5), while model 3 was rejected based on the goodness-of-fit and posterior predictive checks (Fig. 2 d and Fig. S2 g; Δ elpd [model 4 versus 3] = 52.85; SE = 8.74). Model 4 aligns with a recent human in vitro ASDC culture studies, indicating the development of ASDC into DC2 (Sulczewski et al., 2023). Additionally, recent murine findings reinforce the hypothesis of a precursor relationship between ASDC and DC2, as confirmed by the murine ASDC equivalent recently revealed to generate cDC2 (Rodrigues et al., 2023, 2024). While model 4 seems the most biologically probable, lifespan predictions between models 1, 2, and 4 exhibit marginal differences (Fig. 2 e), as do other parameters (Fig. S2, c–f). The proliferation estimates obtained from model 4 indicate that ASDC exhibit the highest proliferation rate (posterior median = 1.03 day^{-1}; Highest Density Interval [HDI] = 0.50–1.52 day^{-1}), followed by DC2 (posterior median = 0.75 day^{-1}; HDI = 0.54–0.92 day^{-1}) and cDC1 (posterior median = 0.49 day^{-1}; HDI = 0.39–0.57 day^{-1}). Moreover, the model predicts the average circulating lifespan of ASDC to be 2.16 days (posterior median; HDI = 1.34–2.96 days), cDC1 1.32 days (posterior median; HDI = 1.02–1.60 days), and DC2 around 2.20 days (posterior median; HDI = 1.95–2.45 days) in the blood (Fig. 2, e and f). This model highlights the ephemeral nature of circulating cDC on their way to lymphoid or non-lymphoid tissue or alternatively to sites of inflammation.

DC3 lifespan in the blood

Next, we investigated the lifespan of circulating DC3. Although human DC3 exhibit overlapping similarities with classical monocytes and DC2, they have been reported to develop independently from ASDC, cDC1, and DC2 (Cytlak et al., 2020). Consequently, we analyzed the kinetics and transition of DC3 in the bone marrow and circulation separately from other cDC populations. Two competing models for DC3 kinetics were proposed in which cells undergo division and acquire labels in the bone marrow before being released into the blood. While model 1 assumes that observed label uptake in DC3 in the blood is due to the proliferation of DC3 in the bone marrow, model 2 explores the possibility of a proliferative precursor (e.g., MDP) in the bone marrow feeding into the DC3 bone marrow pool before being released into the circulation (Fig. 3 a). The mathematical models were fitted to the deuterium-labeled data to estimate the unknown model parameters including proliferation, transition, and differentiation rates in addition to the lifespan of DC3. Bayesian inference for each model was performed to estimate the parameter posterior distributions followed by calculating elpd, which revealed greater support for model 2 over model 1 (Fig. 3 b). Moreover, the posterior predictive plots clearly show that model 1 does not capture the enrichment of the precursor population in the blood compared with model 2. Finally, the proliferation rate in model 2 (Fig. 3 c) closely matched our initial analysis (Fig. 1 e). This model predicts the average circulating lifespan of DC3 to be 2.3 days (posterior median; HDI = 1.42–2.87 days) (Fig. 3, c and d) before cells leave the circulation, presumably by migration into tissues (although death of labeled cells cannot be excluded as an explanation from these data alone).

DC infiltration during acute dermal infection

To probe the relationship between the circulating and tissue cDC compartment and their role during pathology, we developed a simplified human experimental skin blister model (Janela et al., 2019) to sample infiltrating cells to examine the function and kinetics of DC populations in response to a bacterial insult in healthy individuals. An advantage of experimental human models of inflammation compared with the use of clinical samples is the ability to track and trace the inflammatory response from its genesis through to resolution. A blister was

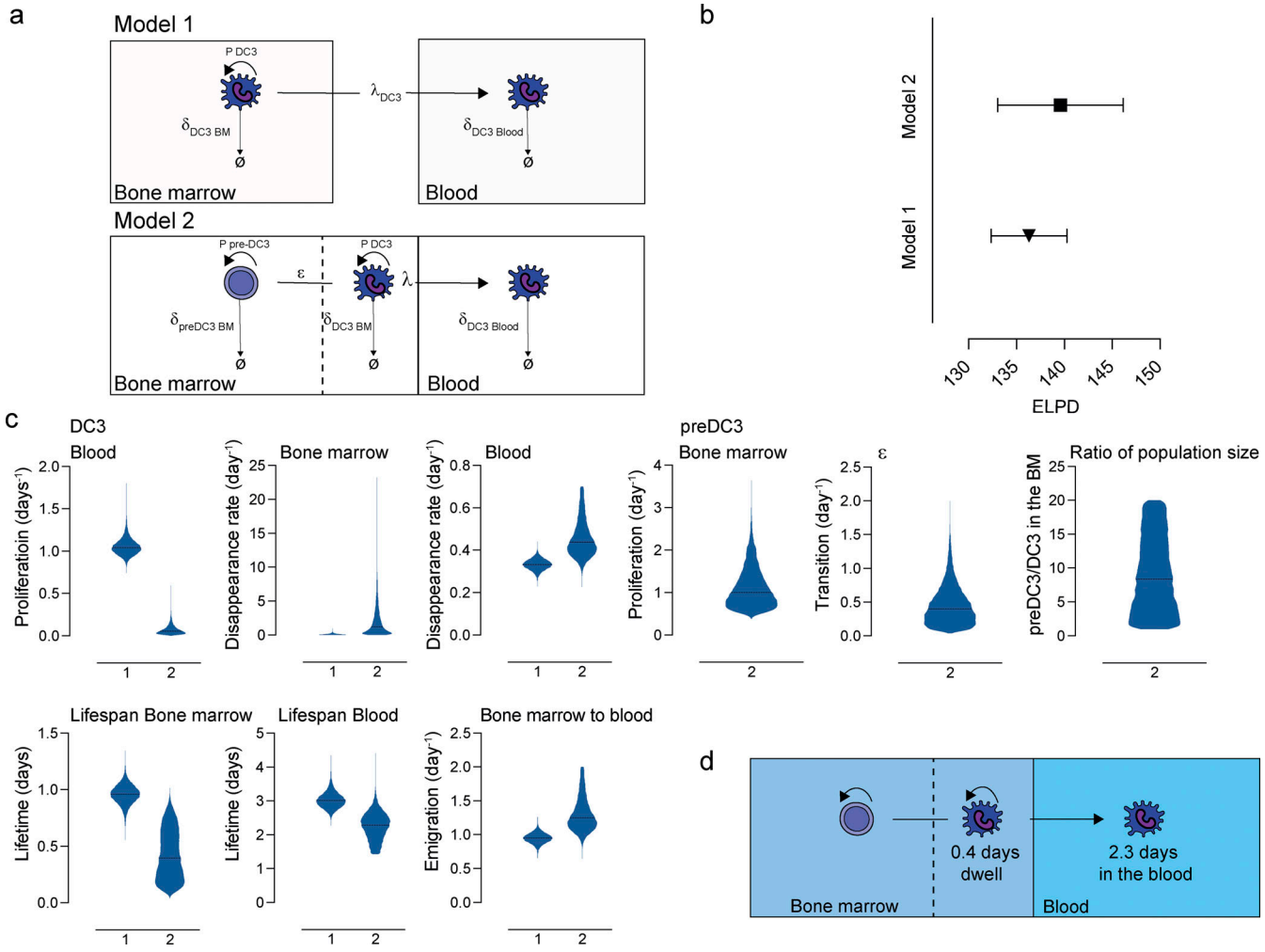

Figure 3. **Model of DC3 developmental kinetics. (a)** Potential models examined to calculate circulating DC3 kinetics. In model 1, DC3 in the bone marrow (BM) may proliferate (P), disappear (δ), or emigrate (λ) into the peripheral circulation. Model 2 is similar to model 1 yet adds a proliferating precursor (PpreDC3) before transitioning (ε) into a DC3 prior to their appearance in the blood. **(b)** Model comparison. The out-of-sample predictiveness taking the form of the elpd ± SD was estimated via PSIS-LOO-CV for single data points for each model. Greater values indicate better relative predictive power of a model, i.e., model 2 performed better than model 1 (note: higher elpd). Comparing the elpd values across models the difference Δ elpd was calculated. **(c)** Marginal posterior distributions of the proliferation rate, disappearance rate, average bone marrow dwell period, average lifespan in the blood, and transition rate were calculated assuming either model 1 or model 2. **(d)** Cartoon depicts the dwell period the bone marrow and peripheral blood lifespan of DC3 for the most likely model (model 2).

elicited 24 or 48 h following an intradermal injection of dead *E. coli* into the forearm of healthy volunteers (Fig. 4 a). This insult provoked a conventional inflammatory response including heat and redness that could be appreciated by the increased blood flow measured by laser Doppler (Fig. 4 b). Not surprisingly, skin biopsies taken 24 h following *E. coli* injection revealed considerable leucocyte infiltration (Fig. 4 c). To assess the composition of this infiltrate, negative pressure blisters were formed over the injection site—24 or 48 h following the *E. coli* injection—and the blister contents were examined by flow cytometry. It was possible to identify all four cDC populations in the blister by 24 h (Fig. 4 d). Due to the presence of overlapping markers between ASDC and pDC, we confirmed the identity of both infiltrating populations. We observed a considerable influx of ASDC to the inflammatory site compared with their circulating blood counterparts (Fig. 4 e). Further investigation examining the differences between blood cDC and their inflammatory equivalent highlighted increased membrane expression of the costimulatory molecule CD80, not just on cDC1, DC2, and DC3 populations but also on ASDC (Fig. 4 f). CD80 expression transiently spikes on ASDC 24 h following the onset of inflammation before rapidly returning to baseline within 48 h. Taken together, these data suggest a unique role for ASDC as an effector cell in their own right when recruited to the site of inflammation. Previously, this population was suggested to act as a mere precursor of the human cDC population. Further investigation is required to specifically appreciate the phenotype of this population at sites of inflammation in human pathology and how inflammation modulates their differentiation and functional potential.

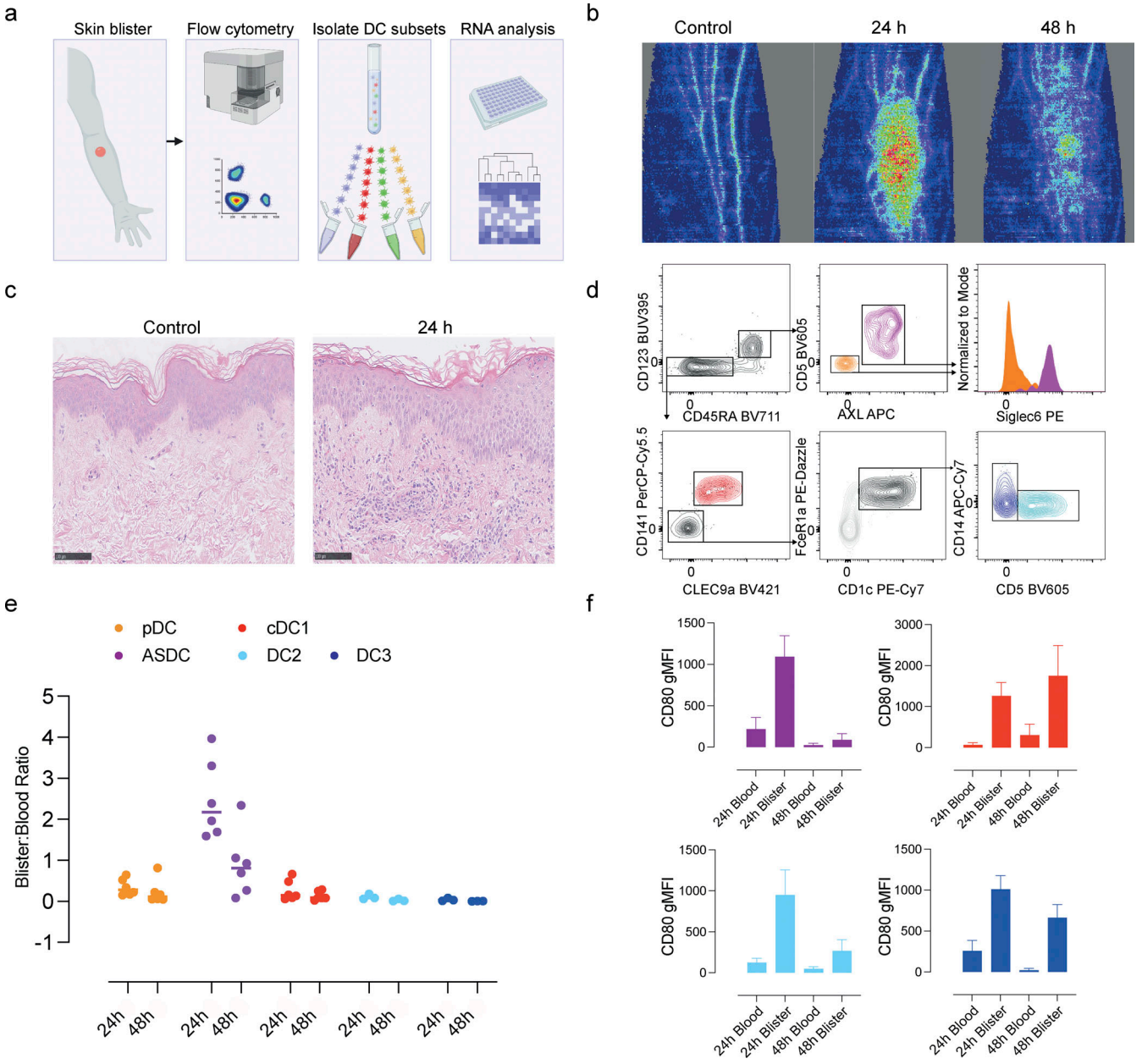

Figure 4. **DC infiltration into the experimental human *E. coli* skin blister. (a)** Protocol of the human experimental skin blister model. This model examines the function and kinetics of DC populations in response to an inflammatory insult in healthy individuals. A skin blister was formed 24 or 48 h following an intradermal injection of 1.5×10^7 UV-killed *E. coli* into the forearm, triggering an acute inflammatory response. The infiltrating cells were isolated and analyzed as described. **(b)** Vascular response at the injection site was assessed by laser Doppler imager capturing flux images. Representative flux images at baseline, 24, and 48 h are shown, representative of $n = 12$. **(c)** Skin biopsies taken 24 h following *E. coli* injection revealed significant leucocyte infiltration compared to control samples, scale bar 100 µm. **(d)** Representative flow cytometry analysis of DC infiltrate following negative pressure blisters formed over the injection site at 24 h ($n = 3$–6 blisters). DC subsets present were identified as pDC (orange), ASDC (purple), cDC1 (red), DC2 (sky blue), and DC3 (navy). **(e)** Blister infiltration at 24 and 48 h following UV-killed *E. coli* injection; data expressed as a ratio blister to blood (cells/ml); $n = 3$–6 independent experiments per time point. **(f)** Expression of co-stimulatory molecule CD80 in blood and infiltrating cDC subsets measure by flow cytometry expressed as geometric mean fluorescence intensity (gMFI), color scheme as above ($n = 3$ independent experiments).

ASDC adopt a unique phenotype during bacterial inflammation

Arrival at the inflammatory site alters infiltrating leucocyte characteristics. Seeking evidence for the potential changes that occur in the infiltrating ASDC population at the site of inflammation and to avoid bias on the relationship between each cDC subset, we examined the infiltrating DC family of cells 24 h following *E. coli* injection by single-cell RNA-sequencing (scRNA-seq). Due to the limited cell numbers acquired from the human blister fluid, we analyzed DC by scRNA-seq using the indexed SMARTseq2 protocol and integrated these data with blood DC from Villani et al. and Dutertre et al. using the Seurat V3 pipeline (Dutertre et al., 2019; See et al., 2017; Villani et al., 2017; GSE94820 and GSE132566). The phenograph algorithm (Levine et al., 2015) identified six phenograph clusters

and calculated differentially expressed genes (DEGs) between these clusters; for a full list of genes see Table S1. This identified DC2 (*CD1C*, *FCER1A*, and *CLEC10A*), pDC (*TCF4*, *LILRA3*, and *GZMB*), cDC1 (*CADM1*, *IDO1*, and *CPVL*), DC3 (*CD163*, *CD14*, *S100A8*), ASDC (*SIGLEC6*, *AXL*, and *CD2*), and mregDC (*CCR7* and *BIRC3*) (Fig. 5, a and b). In addition to RNA expression, indexed protein expression confirmed the identity of these DC subsets (Fig. S3, a and b).

Under steady-state conditions, ASDC have previously been suggested to develop into DC2. Using published gene signatures (See et al., 2017), we extracted genes that are substantially more expressed at the early ASDC stage compared with cDC1 or DC2. Blood ASDC had a significantly higher mean gene signature for these genes compared with blister ASDC (Fig. 5 c). Therefore, we compared the DEG between blood and blister ASDC and as expected identified several proinflammatory genes including *AXL*, *SAT1*, *IFI44L*, and *IL1B* that were upregulated in blister ASDC (Fig. 5 d). We confirmed the increased expression of several of these genes at the protein level, with an increase in CXCR4, CD141, AXL, and CX_3CR1 (Fig. 5 e). In contrast to the transient increase in CD80, a dramatic reduction was observed in several HLA molecules including HLA-A, HLA-DPB2, and HLA-DQ (Fig. 5 d). Pathway analysis revealed that oxidative phosphorylation, interferon signaling, and inflammasome pathways were more prominent in blister ASDC, whilst blood ASDC were enriched in pathways including DC maturation (Fig. 5 f). These data suggest that at the site of inflammation, ASDC adopt a distinct phenotype. To investigate this further, several upregulated genes in blister ASDC including *ISG15*, *IFI44L*, and *IFI27* all pointed toward an activated interferon-β (IFNβ) pathway. We, therefore, tested the impact of IFNβ on ASDC biology, in particular on their antigen presentation capacity, a pathway significantly reduced in blister ASDC (Fig. 5, d and f). Following the incubation with recombinant IFNβ, a trend emerged showing a reduction in HLA molecules, which reached significance with HLA-DQ on ASDC (Fig. 5 g and Fig. S3 c), and this was less pronounced on other cDC populations (Fig. S3, d–f). To assess the expression of IFNβ receptors, we examined *IFNAR1* and *IFNAR2* by scRNA-seq (Fig. S3 g) and protein expression by flow cytometry (Fig. S3 h). These data confirmed the expression of both receptors on ASDC, cDC1, DC2, and DC3. Subsequently, we sought to understand how recombinant IFNβ impacts ASDC interaction and function of allogenic naïve T cells. Of note, untreated ASDC were efficient stimulators of naïve T cells while pDC were the weakest (Fig. 5 h(i)). The presence of IFNβ, however, reduced the capacity of ASDC to stimulate the proliferation of naïve allogenic T cells in the mixed leucocyte reaction. Interestingly, these T cells produced more IL-10 (Fig. 5 h(ii) and Fig. S3 i). Taken together, these data demonstrate that ASDC can adopt an inflammatory phenotype with potential effector functions.

Discussion

Until now, our understanding of cDC kinetics has been largely derived from rodent studies. Previous experiments using the thymidine analog BrdU revealed the rapid integration of BrdU into the splenic cDC compartment, which was attributed to the rapid replenishment of these cells from their circulating precursors (Kamath et al., 2002). This assumption was refined with the observation that murine cDC proliferate in situ, and previous labeling explanations were almost certainly a combination of local proliferation and recent recruitment of blood cDC (Liu et al., 2007) and pre-DC proliferation (Cabeza-Cabrerizo et al., 2019). Parabiosis studies have examined the decay of parabiont-derived cDC in both lymphoid and non-lymphoid organs and demonstrated that cDC recycle over a 2-wk period with a turnover rate of ∼4,300 cells an hour in a lymphoid organ (Ginhoux et al., 2009; Liu et al., 2007). More recently, these rodent studies were performed in a primate setting, with macaque blood cDC being rapidly labeled even before classical monocytes (Sugimoto et al., 2015).

Here, we extended the findings of previous rodent and cercopithecinae studies to a human in vivo setting. Remarkably, labeled ASDC were present within the circulation as early as 6 h following labeling, demonstrating the rapid proliferation and release of these cells into the peripheral circulation. Next, we observed deuterium-labeled blood cDC as early as 1 day after labeling, significantly earlier than we previously observed with classical monocytes (Patel et al., 2017). Interestingly, donor cDC2 have been reported in the blood between 8 and 12 days following allogeneic hematopoietic cell transplantation (McGovern et al., 2014) and dermal DC as early as 14–18 days (Auffermann-Gretzinger et al., 2006; McGovern et al., 2014). Through the creation of four putative models to explore the interplay between ASDC, cDC1, and DC2, it became apparent that the progression of ASDC to DC2 over time was an appropriate trajectory. The DC3 population exhibit several overlapping characteristics with both monocytes and DC2, making them challenging to pigeonhole; previously they were partially hidden within the human classical monocyte gate. This DC3 population shares several monocyte characteristics including the expression of CD14, S100A8, and S100A9 yet lacks the monocyte-defining CD88 membrane receptor (Bourdely et al., 2020; Dutertre et al., 2019). Since their identification, studies indicate DC3 undergo a distinct developmental pathway (Bourdely et al., 2020; Cytlak et al., 2020; Dutertre et al., 2019). Consequently, our data proposed that DC3 arise from a proliferating precursor within the bone marrow before entering circulation, similar to previous rodent studies (Liu et al., 2023). DC2 and DC3 exhibit a similar short lifespan in circulation compared with other leucocyte populations, indicating the ephemeral nature of these cells.

Infection and injury lead to the mobilization of cDC to the site of inflammation. These "inflammatory" DC have been described as a fusion of cDC2 and monocytes (Bosteels et al., 2020); ligation of the Aryl hydrocarbon receptor or viral infections promote $CD14^+$ derived cells to adopt several attributes associated with cDC (Goudot et al., 2017). cDC1 are equipped for the recognition of virally infected, apoptotic or necrotic cells, therefore, cDC1 are efficient cross-presenting cells (Bachem et al., 2010; Canton et al., 2021; Cohn et al., 2013; Crozat et al., 2010; Haniffa et al., 2012; Jongbloed et al., 2010; Mittag et al., 2011; Poulin et al., 2012; Sancho et al., 2008, 2009; Segura et al., 2013a). $CD1c^+$ DC are not just more abundant but also considerably more diverse, as mentioned above this population is composed of DC2/3, equipped with a broad range of C-type lectins, TLRs, RIG-I–like receptors, and NOD-like receptors (Luber et al., 2010) consistent with their likely more prominent role in pathogen sensing. $CD1c^+$ DC are also

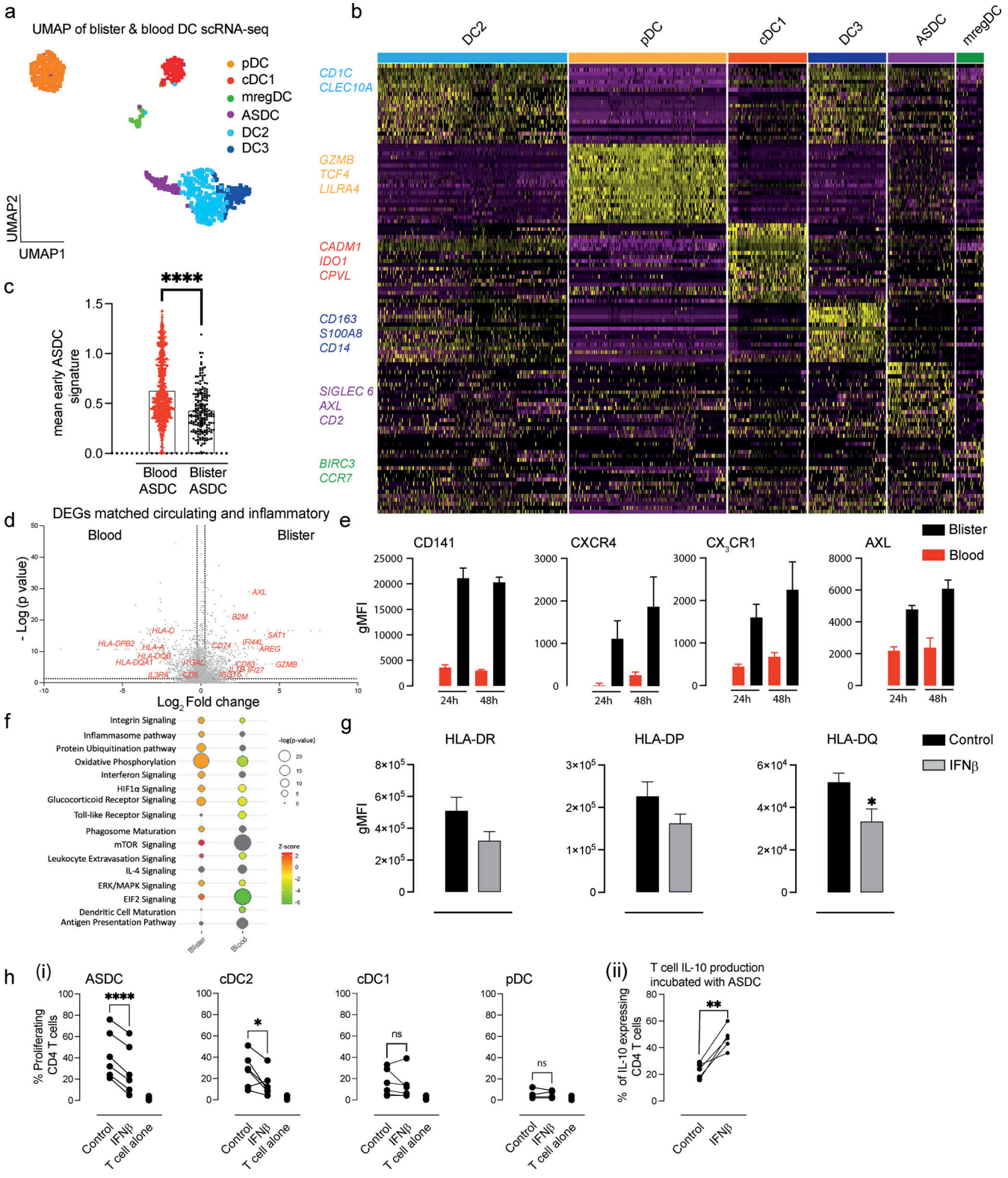

Figure 5. **ASDC adopt a distinct signature at the site of inflammation. (a)** Infiltrating blister cells 24 h following an intradermal injection of 1.5 × 10^7 UV-killed *E. coli* into the forearm were index-sorted and analyzed by scRNA-seq (Smart-seq2) from three volunteers. These data were integrated with published scRNA-seq data from blood DC (Dutertre et al., 2019; Villani et al., 2017) using Seurat V4 pipeline. UMAP of integrated data annotated by phenograph clusters were identified as DC subsets as defined from DEG analysis. **(b)** DEG analysis of phenograph clusters. **(c)** The mean gene expression signature of early ASDC, as defined by See et al. (2017), was analyzed on both blood and blister ASDC. ****P < 0.0001 Mann-Whitney test. **(d)** Volcano plot showing DEGs between blood and blister ASDC. Data shown −Log (P value) against Log_2 fold change. **(e)** Protein expression differences between blood and blister ASDC at both 24 and 48 h after challenge; *n* = 3 blister per time point. **(f)** Ingenuity Pathway Analysis (IPA) demonstrating the enriched pathways associated with blood and blister ASDC.

(g) Analysis of various HLA molecules on ASDC following the incubation with either recombinant IFNβ or vehicle for 20 h and subsequently examined by flow cytometry (n = 6 independent experiments performed in triplicate). *P < 0.05 paired t test. **(h)** Mixed leucocyte reaction (MLR) performed with sorted human cDC1, cDC2, ASDC, and pDC incubated with CFSE-labeled naïve T cells for 6 days. Prior to the addition of T cells, DC were incubated with either vehicle or IFNβ. **(i)** $CD4^+$ T cells were analyzed for their proliferation capacity as a function of their CFSE labeling loss. **(ii)** $CD4^+$ T cells were examined for their intracellular IL-10 expression following MLR. n = 5–8 independent experiments, each performed in triplicate. *P < 0.05, **P < 0.01, and ****P < 0.0001, paired t test.

capable of cross presenting antigens to prime $CD8^+$ T cells (Cohn et al., 2013; Mittag et al., 2011; Segura et al., 2013a), the DC3/DC-like population has been reported to infiltrate solid tumors (Binnewies et al., 2019; Bourdely et al., 2020; Segura et al., 2013b) and adopts inflammatory characteristics in the circulation of lupus patients (Dutertre et al., 2019). Finally, cDC1 have also been observed to help the differentiation of naïve T cells into regulatory cells (Maier et al., 2020). cDC subsets possess exceptional antigen-presenting abilities and high migration capacity, playing a crucial role in infection, vaccination, and tumor biology.

The murine pre-DC population was previously believed to be the circulating precursor for both cDC and pDC; however, this theory was recently challenged with studies showing pDC to have a distinct ontogeny (Dress et al., 2019; Rodrigues et al., 2018). Interestingly, a human challenge model revealed that an infiltrating pDC population and ASDC responded to house dust mite antigen (Chen et al., 2020). Our current findings, which focus on cells recruited to sites of bacterial inflammation highlight how recruited ASDC adopt a unique identity with a distinct IFN signature including *IFI44L* and *IFI27*, reported to be upregulated in myeloid cells in Sjogren's syndrome (Wildenberg et al., 2008). Furthermore, the polyamine catabolic enzyme *SAT1* exhibited heightened expression within the blister ASDC population. *SAT1* functions to diminish cellular spermine, thereby limiting infections, and seems to be regulated by type I IFNs (Mounce et al., 2016). IFNβ appears crucial for resolving the inflammatory response in a model of *E. coli* lung infection (Kumaran Satyanarayanan et al., 2019), possibly attributed to its capacity to modulate HLA expression (Barna et al., 1989). Consistent with these studies, ASDC cultured with recombinant IFNβ adopted a more regulatory phenotype. Blister ASDC preserved their expression of Siglec-6 and AXL, two receptors involved in phagocytosis, that may aid the clearance of the pathogen or required for efferocytosis during the resolution phase of inflammation. These data suggest that ASDC can adapt to become more than precursors. A collection of names are currently in use to describe the ASDC population, including pre-DC (See et al., 2017), DC5 (Villani et al., 2017), and tDC (Leylek et al., 2019). As this DC subset can adopt a distinctive role during inflammation over and above operating as a precursor the term pre-DC should be used appropriately and with caution. In a mouse model of viral influenza, a reduction in cDC1 and cDC2 was observed with an expansion in pDC and tDC—similar to human ASDC—(Leylek et al., 2019) these infiltrating tDC appeared to play a role in murine influenza infection. We observed in the human bacterial skin blister ASDC upregulate their gene expression of *IL1B*, interestingly, in a rodent viral model of M-CoV tDC act as the *IL1B* secreting DC population (Sulczewski et al., 2023). The human ASDC subset is also highly susceptible to HIV infection via Siglec-1 expressed on its membrane; curiously, upon activation, these cells become resistant to infection (Ruffin et al., 2019). Accumulating evidence suggests ASDC represents a highly versatile cell with various context-dependent functions.

Here, we reported on a series of studies investigating the kinetics of human DC subpopulations. The picture that emerges from these data is one in which ASDC are released from the bone marrow almost immediately following mitosis. They do not themselves divide in blood, rather, they either develop into a DC subset or rapidly transit to tissues and draining lymph nodes where, presumably, they develop into cDC (Cabeza-Cabrerizo et al., 2019). When inflammation is provoked, the ASDC subpopulation enters tissues and in this context, assumes an effector phenotype. In the future, it will be vital to examine the trajectory and lifespan of these cells during viral and bacterial infections. These data establish the ephemeral nature of human DC populations and their astonishing plastically in regulating immunity.

Materials and methods

Human blood and bone marrow isolation, subjects, and ethics

Subjects were healthy volunteers or patients undergoing elective orthopedic surgery. All volunteers gave written informed consent, and all studies were conducted according to the principles of the Declaration of Helsinki after approval by the relevant review boards. Deuterium and steady-state studies were conducted under the consent of Hadassah Hospital Ethics Committee 0268-19-HMO and 0367-22 HMO, respectively. Inclusion criteria: adults 18–60 years old, male or female; for women of child-bearing age only, willingness to practice continuous effective contraception during the study. Exclusion criteria included volunteers active or recent infection or febrile illness (<1 mo), active inflammatory or autoimmune condition, recent vaccination (<1 mo), recent surgery (<1 mo), active malignant disease, alcohol intake >36 U/wk (male), >24 U/wk (female), cardiovascular disease, recent blood donation (<1 mo), systemic steroid therapy or use of other immunomodulatory drugs, pregnancy, acquire systemic inflammation during the study, participation in another concurrent research study. Attrition: one subject withdrew after acquiring systemic inflammation during the study. Skin blisters were performed under the consent of University College London, London, UK ethics committee 10527/001 with the same inclusion criteria as the deuterium study. Human bone marrow samples were obtained from patients undergoing orthopedic surgery at Hadassah Medical Center, Jerusalem, Israel, in accordance with Hadassah Hospital Ethics Committee 0785-20-HMO.

Flow cytometry and cell sorting

Peripheral blood mononuclear cells (PBMC) or bone marrow cells were isolated by Ficoll-Paque Plus (GE Healthcare) by density centrifugation (1,000 × g, low acceleration, no brake for 20 min), then resuspended in PBS containing 2% FCS and 2 mM EDTA. Isolated PBMC were incubated with Human Trustain FcX (BioLegend) before antibody labeling as described in the text. A list of antibodies can be found in Table 1. Intracellular and

intranuclear staining was performed in specified experiments following surface staining. Afterward, cells were fixed and permeabilized in fixation buffer and intracellular/nuclear staining permeabilization wash buffer (BioLegend) according to manufacturer instructions prior to incubation with antibodies or 0.5 µg/ml DAPI (BioLegend). LIN was defined as CD3, CD19, CD20, CD66b, NKG2D (CD314), CD88, and CD89. Fluorescence minus one (FMO) was used to define positive populations. Absolute numbers of blood DC subsets were measured using volumetric flow cytometry analysis, and in these studies, 1 ml of whole blood or bone marrow was lysed by ammonium-chloride-potassium before staining for a more accurate cell count. After running the sample (resuspended to 300 µl) on the flow cytometer, the volume acquired was recorded with the cell count, allowing the absolute cells/ml to be calculated. For deuterium studies HLA pre-enrichment (15272HLA; STEMCELL Technologies) was performed (Lubin et al., 2023). Flow cytometry was performed using a BD LSR Fortessa, BD LSR Fortessa X20 (BD Biosciences), or Cytek Aurora (Cytek Biosciences), cell sorting was performed by FACS Aria III (BD Biosciences), and data were analyzed offline using FlowJo version 10 (BD Biosciences).

Cytospin and histology

FACS-sorted DC subsets were resuspended at 5×10^5 cell/ml in PBS and 200 µl of cell suspension was spun at 800 RPM for 8 min Shandon Cytospin 2. Slides were air dried, fixed, and stained with Eosin and Methylene Blue solution (10435310; Thermo Fisher Scientific). A skin punch biopsy (3-mm diameter) was obtained from the site of an *E. coli* injection 24 h later or naïve skin. Baseline biopsies were obtained from the noninjected forearm of volunteers. Biopsies were immediately transferred to neutral buffered formalin for fixation; for further details, see the skin blister section below. Formalin-fixed skin biopsies were embedded in paraffin wax and cut to a thickness of 4 µm. Skin sections were collected on glass slides and stained with Eosin and hematoxylin. Images of the stained slides were obtained using Nanozoom Digital Pathology (NDP) (Hamamatsu) and images were analyzed using NDP.view2 software (Hamamatsu).

Deuterium labeling

Consented healthy volunteers were given 20 g of deuterated glucose (6,6-$^2H_2$-glucose) (Cambridge Isotope Laboratories, Inc.) as an oral solution in half-hourly doses over 3 h, following a priming dose equivalent to 1.8 h dosing at time zero. Blood glucose enrichment was monitored at baseline, and during and after labeling. At selected time points after labeling, DC subsets were stained and sorted by FACS Aria III (BD Biosciences), >5,000 cells for each population were isolated, DNA extracted, and deuterium enrichment measured by GC-MS, as previously described (Busch et al., 2007; Macallan et al., 2009; Patel et al., 2017). Sample size power calculations were performed with previous deuterium kinetics data (Patel et al., 2017) with the aim of sampling enough subjects to have a 95% confidence interval of a desired width when estimating the time at which a peak occurs.

Modeling

To interpret the deuterium labeling, we constructed four competing models of cDC lineage topology in which cells undergo cell division and acquire labels in the bone marrow before being released into the blood (Fig. 2 c). Model 1 explicitly assumes that ASDC may give rise to cDC1 and DC2 in both the bone marrow and blood (See et al., 2017). The model of cell dynamics is defined as follows:

$$\frac{dASDC_{bm}}{dt} = p_{ASDC} * ASDC_{bm} - \delta_{ASDC_{bm}} * ASDC_{bm} - \lambda_{ASDC} * ASDC_{bm} - \Delta_{cDC1_{bm}} * ASDC_{bm} - \Delta_{cDC2_{bm}} * ASDC_{bm}$$

$$\frac{dcDC1_{bm}}{dt} = p_{cDC1} * cDC1_{bm} - \delta_{cDC1_{bm}} * cDC1_{bm} - \lambda_{cDC1} * cDC1_{bm} + \Delta_{cDC1_{bm}} * ASDC_{bm}$$

$$\frac{dDC2_{bm}}{dt} = p_{cDC2} * DC2_{bm} - \delta_{DC2_{bm}} * DC2_{bm} - \lambda_{DC2} * DC2_{bm} + \Delta_{DC2_{bm}} * ASDC_{bm}$$

$$\frac{dASDC_{b}}{dt} = \lambda_{ASDC} * ASDC_{bm} - \delta_{ASDC_{b}} * ASDC_{b} - \Delta_{cDC1_{b}} * ASDC_{b} - \Delta_{DC2_{b}} * ASDC_{b}$$

$$\frac{dcDC1_{b}}{dt} = \lambda_{cDC1} * cDC1_{bm} + \Delta_{cDC1_{b}} * ASDCb - \delta_{cDC1_{b}} * cDC1_{b}$$

$$\frac{dDC2_{b}}{dt} = \lambda_{DC2} * DC2_{bm} + \Delta_{DC2_{b}} * ASDCb - \delta_{DC2_{b}} * DC2_{b}$$

where p_{ASDC}, p_{cDC1}, and p_{cDC2} are the proliferation rates; δ_{ASDCbm}, δ_{cDC1bm}, δ_{DC2bm}, δ_{ASDCb}, δ_{cDC1b}, and δ_{DC2b} are the death/disappearance rates in bone marrow and blood; Δ_{cDC1bm}, Δ_{DC2bm}, Δ_{cDC1b}, and Δ_{DC2bm} are the differentiation rates in bone marrow and blood and λ_{ASDC}, λ_{cDC1}, and λ_{DC2} are the respective transition rates from the bone marrow to blood.

In the presence of deuterium-labeled glucose, deuterium is incorporated into the DNA of dividing DC ($ASDC_{bm}$, $cDC1_{bm}$, $DC2_{bm}$) in the bone marrow. We assume that all populations are at steady state. The relative size of the DC populations in the bone marrow and blood was calculated from data collected (Fig. S1 d). The dynamics of the fraction of labelled cells for each population is then derived and defined as follows:

$$\frac{dLASDC_{bm}}{dt} = p_{ASDC} * c * U(t) - \delta_{ASDC_{bm}} * LASDC_{bm} - \lambda_{ASDC} * LASDC_{bm} - \Delta_{cDC1_{bm}} * LASDC_{bm} - \Delta_{cDC2_{bm}} * LASDC_{bm}$$

$$\frac{dLcDC1_{bm}}{dt} = p_{cDC1} * c * U(t) - \delta_{cDC1bm} * LcDC1_{bm} - \lambda_{cDC1} * LcDC1_{bm} + \Delta_{cDC1bm} * \frac{ASDC_{bm}}{cDC1_{bm}} * LASDC_{bm}$$

$$\frac{dLDC2_{bm}}{dt} = p_{DC2} * c * U(t) - \delta_{DC2_{bm}} * LDC2_{bm} - \lambda_{DC2} * LDC2_{bm} + \Delta_{DC2_{bm}} * \frac{ASDC_{bm}}{DC2_{bm}} * LASDC_{bm}$$

$$\frac{dLASDC_{b}}{dt} = \lambda_{ASDC} * \frac{ASDC_{bm}}{ASDC_{b}} * LASDC_{bm} - \delta_{ASDC_{b}} * LASDC_{b} - \Delta_{cDC1_{b}} * LASDC_{b} - \Delta_{DC2_{b}} * LASDC_{b}$$

$$\frac{dLcDC1_{b}}{dt} = \lambda_{cDC1} * \frac{cDC1_{bm}}{cDC1_{b}} * LcDC1_{bm} + \Delta_{cDC1_{b}} * \frac{ASDC_{b}}{cDC1_{b}} * LASDC_{b} - \delta_{cDC1_{b}} * LcDC1_{b}$$

$$\frac{dLDC2_{b}}{dt} = \lambda_{DC2} * \frac{DC2_{bm}}{DC2_{b}} * LDC2_{bm} + \Delta_{DC2_{b}} * \frac{ASDC_{b}}{DC2_{b}} * LASDC_{b} - \delta_{DC2_{b}} * LDC2_{b}$$

Table 1. **List of antibodies used in this study**

Antigen	Target	Fluorochrome	Clone	Company	Cat. No.
AXL	Human	APC	#108724	R&D Systems	FAB154A
CCR2	Human	PE-Cy7	K036C2	Biolegend	357212
CD11b	Human	PerCP/Cy5.5	ICRF44	Biolegend	301328
CD11c	Human	BV421	B-ly6	BD Biosciences	562561
CD11c	Human	BV786	B-ly6	BD Biosciences	740966
CD11c	Human	PE-Cy7	B-ly6	BD Biosciences	561356
CD11c	Human	V450	B-ly6	BD Biosciences	560370
CD11c	Human	PE-Cy5	3.9	Biolegand	301610
CD123	Human	BUV395	7G3	BD Biosciences	564195
CD123	Human	PerCP/Cy5.5	7G3	BD Biosciences	558714
CD14	Human	BUV805	M5E2	BD Biosciences	612902
CD14	Human	APC-Cy7	M5E2	Biolegend	301820
CD14	Human	FITC	M5E2	Biolegend	301804
CD14	Human	PE	M5E2	Biolegend	301806
CD14	Human	BUV563	M5E2	BD Biosciences	741114
CD141	Human	PE-Dazzle	M80	Biolegend	344120
CD141	Human	PE-Cy7	M80	Biolegend	344110
CD141	Human	PerCP/Cy5.5	M80	Biolegend	344112
CD16	Human	FITC	3G8	Biolegend	302006
CD163	Human	BV785	GHI/61	Biolegend	333632
CD19	Human	PE-Dazzle	HIB19	Biolegend	302252
CD19	Human	FITC	HIB19	Biolegend	302206
CD1c	Human	APC-Cy7	L161	Biolegend	331520
CD1c	Human	BV421	L161	Biolegend	331526
CD1c	Human	BV510	L161	Biolegend	331534
CD1c	Human	BV605	L161	Biolegend	331538
CD1c	Human	PE	L161	Biolegend	331506
CD1c	Human	PE-Cy7	L161	Biolegend	331516
CD1c	Human	BV650	L161	Biolegend	331542
CD2	Human	PE-Cy7	RPA-2.10	Biolegend	300222
CD20	Human	PE-Dazzle	2H7	Biolegend	302348
CD20	Human	FITC	2H7	Biolegend	302304
CD203c	Human	PE	FR3-16A11	Miltenyi Biotec	130 123 512
CD3	Human	FITC	HIT3a	Biolegend	300306
CD3	Human	PE-Dazzle	HIT3a	Biolegend	300336
CD303	Human	BV711	201A	Biolegend	354234
CD303	Human	APC-Cy7	201A	Biolegend	354237
CD33	Human	BV605	P67.6	Biolegend	366612
CD33	Human	BV570	WM53	Biolegend	303417
CD33	Human	BV711	P67.6	Biolegend	366624
CD34	Human	PE Dazzle	581	Biolegend	343534
CD45RA	Human	BV711	HI100	Biolegend	304138
CD5	Human	PE	UCHT2	Biolegend	300608
CD5	Human	PE-Dazzle	UCHT2	Biolegend	300634

Table 1. **List of antibodies used in this study (*Continued*)**

Antigen	Target	Fluorochrome	Clone	Company	Cat. No.
CD5	Human	BV605	L17F12	Biolegend	364020
CD56	Human	PE-Dazzle	QA17A16	Biolegend	392410
CD56	Human	FITC	QA17A16	Biolegend	392414
CD62L	Human	PerCP/Cy5.5	DREG-56	Biolegend	304824
CD66b	Human	AF700	G10F5	Biolegend	305114
CD66b	Human	PE-Dazzle	G10F5	Biolegend	305122
CD66b	Human	FITC	G10F5	Biolegend	305104
CD80	Human	BV605	L307.4	BD Biosciences	563315
CLEC9a	Human	BV421	3A4	BD Biosciences	564266
CLEC9a	Human	PE	8F9	Biolegend	353804
CLEC9a	Human	APC	8F9	Miltenyi Biotec	130 097 368
CX_3CR1	Human	PE	2A9-1	Biolegend	341604
CX_3CR1	Human	PerCP/Cy5.5	2A9-1	Biolegend	341614
CX_3CR1	Human	BUV805	2A9-1	BD Biosciences	749353
FceR1a	Human	PE-Dazzle	AER-37	Biolegend	334634
FceR1a	Human	V510	AER-37	Biolegend	334626
HLA-DR	Human	V500	G46-6	BD Biosciences	561224
HLA-DR	Human	APC-R700	G46-6	BD Biosciences	565127
HLA-DP	Human	BV661	Tu169	BD Biosciences	750943
HLA-DQ	Human	BV480	B7/21	BD Biosciences	746533
IL-10	Human	PE-Dazzle	JES-19F1	Biolegend	506812
INFAR1	Human	PE	85228	Invitrogen	MA5-23630
INFAR2	Human	APC-Vio770	REA124	Miltenyi Biotec	130-099-554
Ki67	Human	PE-Cy7	20Raj1	eBioscience	25-5699-42
NKG2D	Human	PE-Dazzle	1D11	Biolegend	320828
NKG2D	Human	FITC	1D11	Biolegend	320820
Siglec6	Human	FITC	REA852	Miltenyi Biotec	130 112 898
Siglec6	Human	PE	REA852	Miltenyi Biotec	130 112 710
CD163	Human	BV785	GHI/61	Biolegend	333632
CXCR4	Human	PE	12G5	Biolegend	306506

where c(=0.73) (Macallan et al., 2019) is the correction factor for deuterium-labeled glucose and U(t) describes the deuterium-labeled glucose enrichment at time *t* and is defined as two logarithmic growth function accounting for the priming dose during the labeling period with a coupled exponential decay. The parameters of this function were separately determined for each donor by performing maximum likelihood estimation against the deuterium-labeled glucose as measured by finger prick blood samples (Fig. S2 a and Table 2). Considering the steady-state assumption, the model has 10 free parameters to be fitted (p_{ASDCbm}, p_{cDC1bm}, p_{DC2bm}, δ_{ASDCb}, λ_{cDC1}, λ_{DC2}, Δ_{cDC1bm}, Δ_{DC2bm}, Δ_{cDC1b}, Δ_{DC2b}). Additionally, variations of these models were proposed lacking either the release of cDC1 and DC2 into blood, differentiation of ASDC to cDC1, or differentiation occurring in the blood (Fig. 2 c and Fig. S2 b). Similarly, two competing models for the DC3 population were constructed in which cells undergo cell division and acquire labels in the bone marrow before being released into the blood (Fig. 3 a). While model 1 assumes that observed label uptake in DC3 in the blood is due to proliferation of DC3 in the bone marrow, model 2 explores the possibility of proliferative precursor (e.g., MDP) in the bone marrow feeding into DC3 in the bone marrow before being released into the blood. The mathematical models were fitted to deuterium labeling data to estimate the unknown model parameters such as proliferation, transition, and differentiation rates in addition to the lifespan of each DC subset. The SG_2M status (Fig. 1 e and Fig. S1 e) of each subset was used to inform the model's proliferation rate parameters by incorporating it as an informative prior distributions. To derive an approximate daily proliferation rate estimate of each population and construct the prior distribution of a population's proliferation rate in the bone marrow the $S/G_2/M$-phase data was assumed to have

length between 5 and 15 h (Dowling et al., 2014). Then random samples of SG_2M length (5–15 h) (Dowling et al., 2014) as defined by a uniform distribution $U_{[5,15]}$ were combined with 10,000 bootstrapped non-zero samples of the fraction of cells in SG_2M phase, where the proliferation rate p is calculated as

$$p = \left(fraction_{SG_2Mphase} / length_{SG_2Mphase}(h)\right) * 24\,h$$

The prior distribution of the proliferation rates is defined in terms of lognormal distribution and the median proliferation rate for each population was as follows: cDC1 0.2, DC2 0.26, DC3 0.07, and ASDC 0.66 times (Fig. S1 e). The model simulation and Bayesian inference were performed in Julia using DifferentialEquations.jl (Rackauckas and Nie, 2017), ModelingToolkit.jl (Ma et al., 2021, *Preprint*), and Turing.jl (Ge et al., 2018), respectively. The ODEs (ordinary differential equations) were numerically solved using the composite algorithm *AutoTsit5(KenCarp4)* (Kennedy and Carpenter, 2001; Tsitouras, 2011). Turing.jl's implementation of the No-U-Turn sampler was used to obtain samples from the posterior distribution. The goodness-of-fit for each model was quantified by the elpd, which was calculated using PSIS-LOO-CV (Vehtari et al., 2017). Model comparison was performed by comparing the elpd estimates between models as well as visual inspection of posterior predictive model simulations. The model also allows us to calculate the average "dwell time" of a cell in each subset before it undergoes cell death, differentiates, or transitions into a different compartment. The dwell time t_{dwell} is defined as $t_{dwell} = 1/\Sigma(1/\rho_i)$, where ρ is the loss rate due to process i such as death, migration, or differentiation. The code describing the models, fitting the data, and instructions can be found here: https://github.com/jonasmac16/human_dc_lifespan_model.

Human skin blister

1.5×10^7 UV-killed *E. coli* (Strain: NCTC 10418, Source: Public Health England) in 100 µl sterile saline was intradermally injected using a 30-gauge needle into each forearm ~7 cm from the cubital fossa. As a measure of blood flow at the site of inflammation, a laser Doppler image using a mooreLD12Laser Doppler imager (Moor instruments Ltd.) was taken at baseline, 24, and 48 h following injection. A flux image was generated and indicated areas of high and low blood flow. Images were analyzed by moor LDI software v5.2. In a set of studies, skin biopsies were acquired at the site of injection. Local anesthetic (1% lignocaine) was administered at the injection site before a 3-mm punch biopsy was taken using an Acu-Punch 3 mm kit (Schuco). A sterile compress was applied to the site, sutured, and dressed. For the suction blister, a 10-mm-diameter suction blister was induced at either 24 or 48 h after the challenge over the injection site by a negative pressure instrument (NP-4; Electronic diversities Ltd.). After placing the suction chamber over the site, negative pressure was gradually applied from 2 to 10 inches of Hg. Once a blister formed, the pressure was gradually reduced and the blister aspirated. The blister exudate was collected, cells were isolated, and analyzed as described in the text.

scRNA-seq

Following myeloid HLA^+ cell enrichment (STEMCELL Technologies) of whole blood according to the method outlined (Lubin et al., 2023), the cells were subsequently stained and sorted using a FACS ARIA III (BD Biosciences) to isolate cDC; see above. Sorted cells were separated into droplet emulsion using Chromium X (10X Genomics) and scRNA-seq libraries were prepared and barcoded with UDIs using Chromium Next GEM Single Cell 3′ Kit v3.1 (10X Genomics), according to the manufacturer's protocol. Sequencing was performed using Illumina NovaSeq 6000 platform with the following sequencing conditions: 28 bp (Read1) and 90 bp (Read2). Analysis of the 10X Genomics data involved exporting the single cell count matrix from 10X Genomics Cell Ranger version 6.2 and subsequent analysis in R version 4.3.2. Clustering and differential expression analyses were performed using standard functions from Seurat version 5.0.1.

Blister cells were stained for DC subsets and index sorted on FACS ARIA III (BD Biosciences) into a 96-well plate containing lysis buffer, one cell/well using the gating strategy in Fig. S1 a. Plates were sealed and stored at −80°C. Single-cell cDNA libraries were prepared using the SMARTSeq v2 protocol (Picelli et al., 2014) with the following modifications: (i) 1 mg/ml BSA Lysis buffer (Ambionâ; Thermo Fisher Scientific); and (ii) 200 pg cDNA with 1/5 reaction of Illumina Nextera XT kit (Illumina). The length distribution of the cDNA libraries was monitored using a DNA High Sensitivity Reagent Kit on the Perkin Elmer Labchip (Perkin Elmer). All samples were subjected to an indexed paired-end sequencing run of 2 × 151 cycles on an Illumina HiSeq 4000 system (Illumina), with 300 samples/lane.

Preprocessing, quality assessment and control, and analysis of SMARTseq2 single-cell transcriptome data

Paired-end raw reads were aligned to the human reference genome (GRCh38 version 25 release: Gencode) using RSEM

Table 2. **Deuterated glucose dosing schedule**

Time	Time elapsed from first dose (min)	Dose (ml)	Finger prick blood sample
09:00	0	40	✓
09:30	30	10	✓
10:00	60	10	✓
10:30	90	10	
11:00	120	10	✓
11:30	150	10	✓
12:00	180	10	✓
12:30	210		✓
13:00	240		✓
15:00	360		✓
17:00	480		✓
09:00	24 h		✓

The dosing regimen for oral administration of 20 g deuterated glucose resuspended in 100 ml of drinking water. Following an initial 40 ml priming dose, 10 ml was consumed every 30 min thereafter.

version 1.3.0. transcript per million read values were calculated using RSEM and used for downstream analysis. Quality control, selection of highly variable genes, PCA, and differential gene analysis were performed using the Seurat R package. The expression levels of key signature genes by known cell types were used to annotate the cell clusters accordingly. The mean expression of signature genes of early ASDC from See et al. (2017) (GSE98011) was analyzed on blister and blood.

Pathway analysis

Condition-specific DEGs, together with the respective fold-change and P values, were uploaded to the Ingenuity Pathway Analysis (IPA) software (QIAGEN). IPA analysis reported the P value of canonical pathways. Predicted upregulated or downregulated pathways were represented by a positive or negative Z-score, respectively. Canonical pathways determined by IPA's default threshold ($-\log_{10}$ [P value] >1.3) were then shortlisted and bubble plots were used to visualize the P values and Z-scores as previously described in Mulder et al. (2021). Full lists of genes in these pathways can be found in Table S2.

Functional leucocyte assays

DC stimulation: PBMC were isolated as described above and resuspended in Iscove's Modified Dulbecco's Medium (IMDM) (Biological Industries) supplemented with 10% FCS (Biological Industries) in the presence of either vehicle or 100 IU/ml of recombinant IFNβ (R&D Systems) for 20 h in a humidified incubator at 37°C and 5% CO_2. Cells were then stained for flow cytometry and analyzed on a Cytek Aurora. Mixed leucocyte reaction: PBMC were enriched for DC using the Pan-DC enrichment kit (Cat# 130-100-777; Miltenyi) and subsequently FACS-sorted into ASDC, cDC1, cDC2, or pDC. cDC1, cDC2, and pDC acted as a comparison (DC2 and DC3 [cDC2] were grouped together as previous studies have demonstrated these populations have similar proliferation potential towards naïve T cells [Dutertre et al., 2019]). 5,000 FACS-sorted DC subsets were cultured in IMDM, 10% FCS with either vehicle or 100 IU/ml of recombinant IFNβ (R&D Systems) for 12 h in a U-bottom 96-well plate. Next, allogenic naïve T cells were isolated from fresh PBMC using Naive Pan T cell Isolation Kit (Cat# 130-097-095; Miltenyi) and labeled with CFSE (Cat#C34557; Thermo Fisher Scientific) in accordance with the manufacturer's instructions. 50,000 CFSE-labeled Naive Pan T cells were co-cultured with each DC subset or alone. All conditions were performed in triplicate and analysis was performed blinded. At day 6, cells were collected and stained for extracellular and/or intracellular marker expression and analyzed using Cytek Aurora.

Online supplemental material

This information complements the data from Figs. 1, 2, and 5. Fig. S1 provides additional details on the identification of DC populations in the blood and bone marrow, including their quantities within these environments and their proliferation probabilities. Fig. S2 focuses on the deuterium study, covering deuterium enrichment within the plasma, proposed models for each DC population, and the outcomes of these models on various cDC dynamics. It also evaluates how well each model fits the observed data. Fig. S3 complements Fig. 5 by offering further information on the identification of cDC populations by scRNA-seq. This figure also examines the effects of IFNβ on HLA expression on the surface of different cDC populations and how IFNβ influences these DC populations' ability to activate naïve T cells. Table S1 shows the list of DEGs used to identify each DC population. Finally, Table S2 compares ASDC between blood and blister.

Data availability

The scRNA-seq data generated in this study are publicly archived in either the National Center for Biotechnology Information Gene Expression Omnibus database under accession number GSE276518 for blood DC populations or European Molecular Biology Lab-The European Bioinformatics Institute under the accession number E-MTAB-14451 for the index sorted blister cDC. All the codes created for the modeling of DC kinetics are publicly available on Github: https://github.com/jonasmac16/human_dc_lifespan_model.

Acknowledgments

We would like to thank all the volunteers who participated in this study. A special thank you to Jamie Evans, Eleonora Medvedev, and Hadas Segev-Yekutiel for their assistance with cell sorting. We thank Abed Nasereddin and Idit Shiff for their help performing the 10X Genomics, Hebrew University, and the SIgN Immunogenomics Platform for the scRNA-seq profiling of blister samples; Carla Azar and Zvika Granot for their assistance with the cytospin; and the Helsinki committee at the Hadassah Medical Center, Jerusalem. Graphical methods were created with https://BioRender.com.

S. Yona received a startup funding from the Hebrew University and is supported by the Israel Science Foundation Personal Grant (192/20) and Equipment Grant (316/20). A.A. Patel was supported by a PhD Studentship from the Engineering and Physical Sciences Research Council UK research council. R. Lubin is a scholar of the Ariane de Rothschild woman doctoral program. D. Macallan received funding from the Medical Research Council UK (G1001052), The Wellcome Trust (project grant 093053/Z/10/Z), Jefferiss Trust, and Bloodwise (15012). B. Asquith is a Wellcome Trust Investigator (103865). Inclusion and diversity statement: One or more of the authors of this paper received support from a program designed to increase minority representation in science.

Author contributions: R. Lubin: Data curation, Formal analysis, Investigation, Methodology, Project administration, Validation, Visualization, Writing—review & editing, A.A. Patel: Conceptualization, Data curation, Formal analysis, Investigation, Methodology, Software, Validation, Visualization, J. Mackerodt: Data curation, Formal analysis, Methodology, Visualization, Writing—original draft, Writing—review & editing, Y. Zhang: Investigation, R. Gvili: Formal analysis, Investigation, Validation, K. Mulder: Formal analysis, C.-A. Dutertre: Methodology, Supervision, P. Jalali: Investigation, J.R.W. Glanville: Data curation, Investigation, Methodology, Project administration,

Resources, I. Hazan: Writing—review & editing, N. Sridharan: Investigation, G. Rivkin: Investigation, Resources, A. Akarca: Investigation, T. Marafioti: Methodology, D.W. Gilroy: Investigation, Methodology, Resources, L. Kandel: Data curation, Project administration, Resources, A. Mildner: Methodology, Resources, Writing—review & editing, A. Wilensky: Resources, B. Asquith: Data curation, Formal analysis, Investigation, Methodology, Software, Supervision, Validation, Visualization, Writing—review & editing, F. Ginhoux: Resources, D. Macallan: Conceptualization, Data curation, Formal analysis, Investigation, Methodology, Project administration, Supervision, Validation, Visualization, Writing—original draft, Writing—review & editing, S. Yona: Conceptualization, Formal analysis, Funding acquisition, Investigation, Methodology, Project administration, Supervision, Visualization, Writing—original draft, Writing—review & editing.

Disclosures: The authors declare no competing interests exist.

Submitted: 17 May 2022
Revised: 16 July 2024
Accepted: 13 September 2024

References

Auffermann-Gretzinger, S., L. Eger, M. Bornhäuser, K. Schäkel, U. Oelschlaegel, M. Schaich, T. Illmer, C. Thiede, and G. Ehninger. 2006. Fast appearance of donor dendritic cells in human skin: Dynamics of skin and blood dendritic cells after allogeneic hematopoietic cell transplantation. *Transplantation*. 81:866–873. https://doi.org/10.1097/01.tp.0000203318.16224.57

Bachem, A., S. Güttler, E. Hartung, F. Ebstein, M. Schaefer, A. Tannert, A. Salama, K. Movassaghi, C. Opitz, H.W. Mages, et al. 2010. Superior antigen cross-presentation and XCR1 expression define human CD11c+CD141+ cells as homologues of mouse CD8+ dendritic cells. *J. Exp. Med.* 207:1273–1281. https://doi.org/10.1084/jem.20100348

Barna, B.P., S.M. Chou, B. Jacobs, B. Yen-Lieberman, and R.M. Ransohoff. 1989. Interferon-beta impairs induction of HLA-DR antigen expression in cultured adult human astrocytes. *J. Neuroimmunol.* 23:45–53. https://doi.org/10.1016/0165-5728(89)90072-6

Binnewies, M., A.M. Mujal, J.L. Pollack, A.J. Combes, E.A. Hardison, K.C. Barry, J. Tsui, M.K. Ruhland, K. Kersten, M.A. Abushawish, et al. 2019. Unleashing type-2 dendritic cells to drive protective antitumor CD4$^+$ T cell immunity. *Cell*. 177:556–571.e16. https://doi.org/10.1016/j.cell.2019.02.005

Bosteels, C., K. Neyt, M. Vanheerswynghels, M.J. van Helden, D. Sichien, N. Debeuf, S. De Prijck, V. Bosteels, N. Vandamme, L. Martens, et al. 2020. Inflammatory type 2 cDCs acquire features of cDC1s and macrophages to orchestrate immunity to respiratory virus infection. *Immunity*. 52:1039–1056.e9. https://doi.org/10.1016/j.immuni.2020.04.005

Bourdely, P., G. Anselmi, K. Vaivode, R.N. Ramos, Y. Missolo-Koussou, S. Hidalgo, J. Tosselo, N. Nuñez, W. Richer, A. Vincent-Salomon, et al. 2020. Transcriptional and functional analysis of CD1c$^+$ human dendritic cells identifies a CD163$^+$ subset priming CD8$^+$CD103$^+$ T cells. *Immunity*. 53:335–352.e8. https://doi.org/10.1016/j.immuni.2020.06.002

Breton, G., J. Lee, K. Liu, and M.C. Nussenzweig. 2015. Defining human dendritic cell progenitors by multiparametric flow cytometry. *Nat. Protoc.* 10:1407–1422. https://doi.org/10.1038/nprot.2015.092

Busch, R., R.A. Neese, M. Awada, G.M. Hayes, and M.K. Hellerstein. 2007. Measurement of cell proliferation by heavy water labeling. *Nat. Protoc.* 2:3045–3057. https://doi.org/10.1038/nprot.2007.420

Cabeza-Cabrerizo, M., J. van Blijswijk, S. Wienert, D. Heim, R.P. Jenkins, P. Chakravarty, N. Rogers, B. Frederico, S. Acton, E. Beerling, et al. 2019. Tissue clonality of dendritic cell subsets and emergency DCpoiesis revealed by multicolor fate mapping of DC progenitors. *Sci. Immunol.* 4:eaaw1941. https://doi.org/10.1126/sciimmunol.aaw1941

Canton, J., H. Blees, C.M. Henry, M.D. Buck, O. Schulz, N.C. Rogers, E. Childs, S. Zelenay, H. Rhys, M.C. Domart, et al. 2021. The receptor DNGR-1 signals for phagosomal rupture to promote cross-presentation of dead-cell-associated antigens. *Nat. Immunol.* 22:140–153. https://doi.org/10.1038/s41590-020-00824-x

Chen, Y.L., T. Gomes, C.S. Hardman, F.A. Vieira Braga, D. Gutowska-Owsiak, M. Salimi, N. Gray, D.A. Duncan, G. Reynolds, D. Johnson, et al. 2020. Re-evaluation of human BDCA-2+ DC during acute sterile skin inflammation. *J. Exp. Med.* 217:jem.20190811. https://doi.org/10.1084/jem.20190811

Cohn, L., B. Chatterjee, F. Esselborn, A. Smed-Sörensen, N. Nakamura, C. Chalouni, B.C. Lee, R. Vandlen, T. Keler, P. Lauer, et al. 2013. Antigen delivery to early endosomes eliminates the superiority of human blood BDCA3+ dendritic cells at cross presentation. *J. Exp. Med.* 210:1049–1063. https://doi.org/10.1084/jem.20121251

Cossarizza, A., H.D. Chang, A. Radbruch, S. Abrignani, R. Addo, M. Akdis, I. Andra, F. Andreata, F. Annunziato, E. Arranz, et al., and J. Yang. 2021. Guidelines for the use of flow cytometry and cell sorting in immunological studies (third edition). *Eur. J. Immunol.* 51:2708–3145. https://doi.org/10.1002/eji.202170126

Crozat, K., R. Guiton, V. Contreras, V. Feuillet, C.A. Dutertre, E. Ventre, T.P. Vu Manh, T. Baranek, A.K. Storset, J. Marvel, et al. 2010. The XC chemokine receptor 1 is a conserved selective marker of mammalian cells homologous to mouse CD8alpha+ dendritic cells. *J. Exp. Med.* 207:1283–1292. https://doi.org/10.1084/jem.20100223

Cytlak, U., A. Resteu, S. Pagan, K. Green, P. Milne, S. Maisuria, D. McDonald, G. Hulme, A. Filby, B. Carpenter, et al. 2020. Differential IRF8 transcription factor requirement defines two pathways of dendritic cell development in humans. *Immunity*. 53:353–370.e8. https://doi.org/10.1016/j.immuni.2020.07.003

Diao, J., E. Winter, W. Chen, C. Cantin, and M.S. Cattral. 2004. Characterization of distinct conventional and plasmacytoid dendritic cell-committed precursors in murine bone marrow. *J. Immunol.* 173:1826–1833. https://doi.org/10.4049/jimmunol.173.3.1826

Dowling, M.R., A. Kan, S. Heinzel, J.H. Zhou, J.M. Marchingo, C.J. Wellard, J.F. Markham, and P.D. Hodgkin. 2014. Stretched cell cycle model for proliferating lymphocytes. *Proc. Natl. Acad. Sci. USA*. 111:6377–6382. https://doi.org/10.1073/pnas.1322420111

Dress, R.J., C.A. Dutertre, A. Giladi, A. Schlitzer, I. Low, N.B. Shadan, A. Tay, J. Lum, M.F.B.M. Kairi, Y.Y. Hwang, et al. 2019. Plasmacytoid dendritic cells develop from Ly6D$^+$ lymphoid progenitors distinct from the myeloid lineage. *Nat. Immunol.* 20:852–864. https://doi.org/10.1038/s41590-019-0420-3

Dutertre, C.A., E. Becht, S.E. Irac, A. Khalilnezhad, V. Narang, S. Khalilnezhad, P.Y. Ng, L.L. van den Hoogen, J.Y. Leong, B. Lee, et al. 2019. Single-cell analysis of human mononuclear phagocytes reveals subset-defining markers and identifies circulating inflammatory dendritic cells. *Immunity*. 51:573–589.e8. https://doi.org/10.1016/j.immuni.2019.08.008

Fogg, D.K., C. Sibon, C. Miled, S. Jung, P. Aucouturier, D.R. Littman, A. Cumano, and F. Geissmann. 2006. A clonogenic bone marrow progenitor specific for macrophages and dendritic cells. *Science*. 311:83–87. https://doi.org/10.1126/science.1117729

Ge, H., K. Xu, and Z. Ghahramani. 2018. Turing: A language for flexible probabilistic inference. Proceedings of the Twenty-First International Conference on Artificial Intelligence and Statistics. 84:1682–1690

Ginhoux, F., M. Guilliams, and M. Merad. 2022. Expanding dendritic cell nomenclature in the single-cell era. *Nat. Rev. Immunol.* 22:67–68. https://doi.org/10.1038/s41577-022-00675-7

Ginhoux, F., K. Liu, J. Helft, M. Bogunovic, M. Greter, D. Hashimoto, J. Price, N. Yin, J. Bromberg, S.A. Lira, et al. 2009. The origin and development of nonlymphoid tissue CD103+ DCs. *J. Exp. Med.* 206:3115–3130. https://doi.org/10.1084/jem.20091756

Goudot, C., A. Coillard, A.C. Villani, P. Gueguen, A. Cros, S. Sarkizova, T.L. Tang-Huau, M. Bohec, S. Baulande, N. Hacohen, et al. 2017. Aryl hydrocarbon receptor controls monocyte differentiation into dendritic cells versus macrophages. *Immunity*. 47:582–596.e6. https://doi.org/10.1016/j.immuni.2017.08.016

Grajales-Reyes, G.E., A. Iwata, J. Albring, X. Wu, R. Tussiwand, W. Kc, N.M. Kretzer, C.G. Briseño, V. Durai, P. Bagadia, et al. 2015. Batf3 maintains autoactivation of Irf8 for commitment of a CD8α(+) conventional DC clonogenic progenitor. *Nat. Immunol.* 16:708–717. https://doi.org/10.1038/ni.3197

Guilliams, M., F. Ginhoux, C. Jakubzick, S.H. Naik, N. Onai, B.U. Schraml, E. Segura, R. Tussiwand, and S. Yona. 2014. Dendritic cells, monocytes and macrophages: A unified nomenclature based on ontogeny. *Nat. Rev. Immunol.* 14:571–578. https://doi.org/10.1038/nri3712

Guilliams, M., A. Mildner, and S. Yona. 2018. Developmental and functional heterogeneity of monocytes. *Immunity*. 49:595–613. https://doi.org/10.1016/j.immuni.2018.10.005

Haniffa, M., A. Shin, V. Bigley, N. McGovern, P. Teo, P. See, P.S. Wasan, X.N. Wang, F. Malinarich, B. Malleret, et al. 2012. Human tissues contain CD141hi cross-presenting dendritic cells with functional homology to mouse CD103+ nonlymphoid dendritic cells. *Immunity*. 37:60–73. https://doi.org/10.1016/j.immuni.2012.04.012

Jackson, J.T., Y. Hu, R. Liu, F. Masson, A. D'Amico, S. Carotta, A. Xin, M.J. Camilleri, A.M. Mount, A. Kallies, et al. 2011. Id2 expression delineates differential checkpoints in the genetic program of CD8α+ and CD103+ dendritic cell lineages. *EMBO J.* 30:2690–2704. https://doi.org/10.1038/emboj.2011.163

Janela, B., A.A. Patel, M.C. Lau, C.C. Goh, R. Msallam, W.T. Kong, M. Fehlings, S. Hubert, J. Lum, Y. Simoni, et al. 2019. A subset of type I conventional dendritic cells controls cutaneous bacterial infections through VEGFα-mediated recruitment of neutrophils. *Immunity*. 50:1069–1083.e8. https://doi.org/10.1016/j.immuni.2019.03.001

Jongbloed, S.L., A.J. Kassianos, K.J. McDonald, G.J. Clark, X. Ju, C.E. Angel, C.J. Chen, P.R. Dunbar, R.B. Wadley, V. Jeet, et al. 2010. Human CD141+ (BDCA-3)+ dendritic cells (DCs) represent a unique myeloid DC subset that cross-presents necrotic cell antigens. *J. Exp. Med.* 207:1247–1260. https://doi.org/10.1084/jem.20092140

Kamath, A.T., S. Henri, F. Battye, D.F. Tough, and K. Shortman. 2002. Developmental kinetics and lifespan of dendritic cells in mouse lymphoid organs. *Blood*. 100:1734–1741. https://doi.org/10.1182/blood.V100.5.1734.h81702001734_1734_1741

Kennedy, C.A., and M. Carpenter. 2001. Additive Runge-Kutta Schemes for Convection-Diffusion-Reaction Equations. *In NASA/TM; 2001-211038*. National Aeronautics and Space Administration, Langley Research Center, Hampton, VA, USA.

Kumaran Satyanarayanan, S., D. El Kebir, S. Soboh, S. Butenko, M. Sekheri, J. Saadi, N. Peled, S. Assi, A. Othman, S. Schif-Zuck, et al. 2019. IFN-β is a macrophage-derived effector cytokine facilitating the resolution of bacterial inflammation. *Nat. Commun.* 10:3471. https://doi.org/10.1038/s41467-019-10903-9

Kvedaraite, E., and F. Ginhoux. 2022. Human dendritic cells in cancer. *Sci. Immunol.* 7:eabm9409. https://doi.org/10.1126/sciimmunol.abm9409

Lahoz-Beneytez, J., M. Elemans, Y. Zhang, R. Ahmed, A. Salam, M. Block, C. Niederalt, B. Asquith, and D. Macallan. 2016. Human neutrophil kinetics: Modeling of stable isotope labeling data supports short blood neutrophil half-lives. *Blood*. 127:3431–3438. https://doi.org/10.1182/blood-2016-03-700336

Lee, J., G. Breton, T.Y. Oliveira, Y.J. Zhou, A. Aljoufi, S. Puhr, M.J. Cameron, R.P. Sékaly, M.C. Nussenzweig, and K. Liu. 2015. Restricted dendritic cell and monocyte progenitors in human cord blood and bone marrow. *J. Exp. Med.* 212:385–399. https://doi.org/10.1084/jem.20141442

Levine, J.H., E.F. Simonds, S.C. Bendall, K.L. Davis, A.D. Amir, M.D. Tadmor, O. Litvin, H.G. Fienberg, A. Jager, E.R. Zunder, et al. 2015. Data-driven phenotypic dissection of AML reveals progenitor-like cells that correlate with prognosis. *Cell*. 162:184–197. https://doi.org/10.1016/j.cell.2015.05.047

Leylek, R., M. Alcántara-Hernández, Z. Lanzar, A. Lüdtke, O.A. Perez, B. Reizis, and J. Idoyaga. 2019. Integrated cross-species analysis identifies a conserved transitional dendritic cell population. *Cell Rep.* 29:3736–3750.e8. https://doi.org/10.1016/j.celrep.2019.11.042

Liu, K., G.D. Victora, T.A. Schwickert, P. Guermonprez, M.M. Meredith, K. Yao, F.F. Chu, G.J. Randolph, A.Y. Rudensky, and M. Nussenzweig. 2009. In vivo analysis of dendritic cell development and homeostasis. *Science*. 324:392–397. https://doi.org/10.1126/science.1170540

Liu, K., C. Waskow, X. Liu, K. Yao, J. Hoh, and M. Nussenzweig. 2007. Origin of dendritic cells in peripheral lymphoid organs of mice. *Nat. Immunol.* 8:578–583. https://doi.org/10.1038/ni1462

Liu, Z., H. Wang, Z. Li, R.J. Dress, Y. Zhu, S. Zhang, D. De Feo, W.T. Kong, P. Cai, A. Shin, et al. 2023. Dendritic cell type 3 arises from Ly6C(+) monocyte-dendritic cell progenitors. *Immunity*. 56:1761–1777 e1766.

Luber, C.A., J. Cox, H. Lauterbach, B. Fancke, M. Selbach, J. Tschopp, S. Akira, M. Wiegand, H. Hochrein, M. O'Keeffe, and M. Mann. 2010. Quantitative proteomics reveals subset-specific viral recognition in dendritic cells. *Immunity*. 32:279–289. https://doi.org/10.1016/j.immuni.2010.01.013

Lubin, R., R. Gvili, I. Hazan, and S. Yona. 2023. Human dendritic cell enrichment and their activation of T cells. *Curr. Protoc.* 3:e873. https://doi.org/10.1002/cpz1.873

Ma, Y., S. Gowda, R. Anantharaman, C. Laughman, V. Shah, and C. Rackauckas. 2021. ModelingToolkit: A composable graph transformation system for equation-based modeling. *arXiv*. https://doi.org/10.48550/arXiv.2103.05244 (Preprint posted March 9, 2021).

Macallan, D.C., B. Asquith, Y. Zhang, C. de Lara, H. Ghattas, J. Defoiche, and P.C. Beverley. 2009. Measurement of proliferation and disappearance of rapid turnover cell populations in human studies using deuterium-labeled glucose. *Nat. Protoc.* 4:1313–1327. https://doi.org/10.1038/nprot.2009.117

Macallan, D.C., R. Busch, and B. Asquith. 2019. Current estimates of T cell kinetics in humans. *Curr. Opin. Syst. Biol.* 18:77–86. https://doi.org/10.1016/j.coisb.2019.10.002

Maier, B., A.M. Leader, S.T. Chen, N. Tung, C. Chang, J. LeBerichel, A. Chudnovskiy, S. Maskey, L. Walker, J.P. Finnigan, et al. 2020. A conserved dendritic-cell regulatory program limits antitumour immunity. *Nature*. 580:257–262. https://doi.org/10.1038/s41586-020-2134-y

McGovern, N., A. Schlitzer, M. Gunawan, L. Jardine, A. Shin, E. Poyner, K. Green, R. Dickinson, X.N. Wang, D. Low, et al. 2014. Human dermal CD14⁺ cells are a transient population of monocyte-derived macrophages. *Immunity*. 41:465–477. https://doi.org/10.1016/j.immuni.2014.08.006

Mittag, D., A.I. Proietto, T. Loudovaris, S.I. Mannering, D. Vremec, K. Shortman, L. Wu, and L.C. Harrison. 2011. Human dendritic cell subsets from spleen and blood are similar in phenotype and function but modified by donor health status. *J. Immunol.* 186:6207–6217. https://doi.org/10.4049/jimmunol.1002632

Mounce, B.C., E.Z. Poirier, G. Passoni, E. Simon-Loriere, T. Cesaro, M. Prot, K.A. Stapleford, G. Moratorio, A. Sakuntabhai, J.P. Levraud, and M. Vignuzzi. 2016. Interferon-induced spermidine-spermine acetyltransferase and polyamine depletion restrict zika and chikungunya viruses. *Cell Host Microbe*. 20:167–177. https://doi.org/10.1016/j.chom.2016.06.011

Mulder, K., A.A. Patel, W.T. Kong, C. Piot, E. Halitzki, G. Dunsmore, S. Khalilnezhad, S.E. Irac, A. Dubuisson, M. Chevrier, et al. 2021. Cross-tissue single-cell landscape of human monocytes and macrophages in health and disease. *Immunity*. 54:1883–1900.e5. https://doi.org/10.1016/j.immuni.2021.07.007

Naik, S.H., D. Metcalf, A. van Nieuwenhuijze, I. Wicks, L. Wu, M. O'Keeffe, and K. Shortman. 2006. Intrasplenic steady-state dendritic cell precursors that are distinct from monocytes. *Nat. Immunol.* 7:663–671. https://doi.org/10.1038/ni1340

Naik, S.H., P. Sathe, H.Y. Park, D. Metcalf, A.I. Proietto, A. Dakic, S. Carotta, M. O'Keeffe, M. Bahlo, A. Papenfuss, et al. 2007. Development of plasmacytoid and conventional dendritic cell subtypes from single precursor cells derived in vitro and in vivo. *Nat. Immunol.* 8:1217–1226. https://doi.org/10.1038/ni1522

Nussenzweig, M.C., and R.M. Steinman. 1980. Contribution of dendritic cells to stimulation of the murine syngeneic mixed leukocyte reaction. *J. Exp. Med.* 151:1196–1212. https://doi.org/10.1084/jem.151.5.1196

Onai, N., A. Obata-Onai, M.A. Schmid, T. Ohteki, D. Jarrossay, and M.G. Manz. 2007. Identification of clonogenic common Flt3+M-CSFR+ plasmacytoid and conventional dendritic cell progenitors in mouse bone marrow. *Nat. Immunol.* 8:1207–1216. https://doi.org/10.1038/ni1518

Patel, A.A., F. Ginhoux, and S. Yona. 2021. Monocytes, macrophages, dendritic cells and neutrophils: An update on lifespan kinetics in health and disease. *Immunology*. 163:250–261. https://doi.org/10.1111/imm.13320

Patel, A.A., Y. Zhang, J.N. Fullerton, L. Boelen, A. Rongvaux, A.A. Maini, V. Bigley, R.A. Flavell, D.W. Gilroy, B. Asquith, et al. 2017. The fate and lifespan of human monocyte subsets in steady state and systemic inflammation. *J. Exp. Med.* 214:1913–1923. https://doi.org/10.1084/jem.20170355

Picelli, S., O.R. Faridani, A.K. Björklund, G. Winberg, S. Sagasser, and R. Sandberg. 2014. Full-length RNA-seq from single cells using Smart-seq2. *Nat. Protoc.* 9:171–181. https://doi.org/10.1038/nprot.2014.006

Poulin, L.F., Y. Reyal, H. Uronen-Hansson, B.U. Schraml, D. Sancho, K.M. Murphy, U.K. Håkansson, L.F. Moita, W.W. Agace, D. Bonnet, and C. Reis e Sousa. 2012. DNGR-1 is a specific and universal marker of mouse and human Batf3-dependent dendritic cells in lymphoid and non-lymphoid tissues. *Blood*. 119:6052–6062. https://doi.org/10.1182/blood-2012-01-406967

Rackauckas, C., and Q. Nie. 2017. DifferentialEquations.jl—a performant and feature-rich ecosystem for solving differential equations in Julia. *J. Open Res. Softw.* 5:15–25. https://doi.org/10.5334/jors.151

Rodrigues, P.F., L. Alberti-Servera, A. Eremin, G.E. Grajales-Reyes, R. Ivanek, and R. Tussiwand. 2018. Distinct progenitor lineages contribute to the

heterogeneity of plasmacytoid dendritic cells. *Nat. Immunol.* 19:711–722. https://doi.org/10.1038/s41590-018-0136-9

Rodrigues, P.F., A. Kouklas, G. Cvijetic, N. Bouladoux, M. Mitrovic, J.V. Desai, D.S. Lima-Junior, M.S. Lionakis, Y. Belkaid, R. Ivanek, and R. Tussiwand. 2023. pDC-like cells are pre-DC2 and require KLF4 to control homeostatic CD4 T cells. *Sci. Immunol.* 8:eadd4132. https://doi.org/10.1126/sciimmunol.add4132

Rodrigues, P.F., T. Trsan, G. Cvijetic, D. Khantakova, S.K. Panda, Z. Liu, F. Ginhoux, M. Cella, and M. Colonna. 2024. Progenitors of distinct lineages shape the diversity of mature type 2 conventional dendritic cells. *Immunity*. 57:1567–1585.e5. https://doi.org/10.1016/j.immuni.2024.05.007

Ruffin, N., E. Gea-Mallorquí, F. Brouiller, M. Jouve, A. Silvin, P. See, C.A. Dutertre, F. Ginhoux, and P. Benaroch. 2019. Constitutive Siglec-1 expression confers susceptibility to HIV-1 infection of human dendritic cell precursors. *Proc. Natl. Acad. Sci. USA*. 116:21685–21693. https://doi.org/10.1073/pnas.1911007116

Sancho, D., O.P. Joffre, A.M. Keller, N.C. Rogers, D. Martínez, P. Hernanz-Falcón, I. Rosewell, and C. Reis e Sousa. 2009. Identification of a dendritic cell receptor that couples sensing of necrosis to immunity. *Nature*. 458:899–903. https://doi.org/10.1038/nature07750

Sancho, D., D. Mourão-Sá, O.P. Joffre, O. Schulz, N.C. Rogers, D.J. Pennington, J.R. Carlyle, and C. Reis e Sousa. 2008. Tumor therapy in mice via antigen targeting to a novel, DC-restricted C-type lectin. *J. Clin. Invest.* 118:2098–2110. https://doi.org/10.1172/JCI34584

Schlitzer, A., V. Sivakamasundari, J. Chen, H.R. Sumatoh, J. Schreuder, J. Lum, B. Malleret, S. Zhang, A. Larbi, F. Zolezzi, et al. 2015. Identification of cDC1- and cDC2-committed DC progenitors reveals early lineage priming at the common DC progenitor stage in the bone marrow. *Nat. Immunol.* 16:718–728. https://doi.org/10.1038/ni.3200

Schraml, B.U., J. van Blijswijk, S. Zelenay, P.G. Whitney, A. Filby, S.E. Acton, N.C. Rogers, N. Moncaut, J.J. Carvajal, and C. Reis e Sousa. 2013. Genetic tracing via DNGR-1 expression history defines dendritic cells as a hematopoietic lineage. *Cell*. 154:843–858. https://doi.org/10.1016/j.cell.2013.07.014

See, P., C.A. Dutertre, J. Chen, P. Günther, N. McGovern, S.E. Irac, M. Gunawan, M. Beyer, K. Händler, K. Duan, et al. 2017. Mapping the human DC lineage through the integration of high-dimensional techniques. *Science*. 356:eaag3009. https://doi.org/10.1126/science.aag3009

Segura, E., M. Durand, and S. Amigorena. 2013a. Similar antigen cross-presentation capacity and phagocytic functions in all freshly isolated human lymphoid organ-resident dendritic cells. *J. Exp. Med.* 210:1035–1047. https://doi.org/10.1084/jem.20121103

Segura, E., M. Touzot, A. Bohineust, A. Cappuccio, G. Chiocchia, A. Hosmalin, M. Dalod, V. Soumelis, and S. Amigorena. 2013b. Human inflammatory dendritic cells induce Th17 cell differentiation. *Immunity*. 38:336–348. https://doi.org/10.1016/j.immuni.2012.10.018

Sugimoto, C., A. Hasegawa, Y. Saito, Y. Fukuyo, K.B. Chiu, Y. Cai, M.W. Breed, K. Mori, C.J. Roy, A.A. Lackner, et al. 2015. Differentiation kinetics of blood monocytes and dendritic cells in macaques: Insights to understanding human myeloid cell development. *J. Immunol.* 195:1774–1781. https://doi.org/10.4049/jimmunol.1500522

Sulczewski, F.B., R.A. Maqueda-Alfaro, M. Alcántara-Hernández, O.A. Perez, S. Saravanan, T.J. Yun, D. Seong, R. Arroyo Hornero, H.M. Raquer-McKay, E. Esteva, et al. 2023. Transitional dendritic cells are distinct from conventional DC2 precursors and mediate proinflammatory antiviral responses. *Nat. Immunol.* 24:1265–1280. https://doi.org/10.1038/s41590-023-01545-7

Tak, T., J. Drylewicz, L. Conemans, R.J. de Boer, L. Koenderman, J.A.M. Borghans, and K. Tesselaar. 2017. Circulatory and maturation kinetics of human monocyte subsets in vivo. *Blood*. 130:1474–1477. https://doi.org/10.1182/blood-2017-03-771261

Toyama-Sorimachi, N., Y. Omatsu, A. Onoda, Y. Tsujimura, T. Iyoda, A. Kikuchi-Maki, H. Sorimachi, T. Dohi, S. Taki, K. Inaba, and H. Karasuyama. 2005. Inhibitory NK receptor Ly49Q is expressed on subsets of dendritic cells in a cellular maturation- and cytokine stimulation-dependent manner. *J. Immunol.* 174:4621–4629. https://doi.org/10.4049/jimmunol.174.8.4621

Tsitouras, C. 2011. Runge-Kutta pairs of order 5(4) satisfying only the first column simplifying assumption. *Comput. Math. Appl.* 62:770–775. https://doi.org/10.1016/j.camwa.2011.06.002

Tussiwand, R., P. Guermonprez, and S. Yona. 2023. Dendritic cells. *In* Paul's Fundamental Immunology. Eighth edition. M.F. Flajnik, N.J. Singh, and S.M. Holland, editors. Lippincott Willaims and Wilkins, Philadelphia, PA, USA. 1034–1053.

Vehtari, A., A. Gelman, and J. Gabry. 2017. Practical Bayesian model evaluation using leave-one-out cross-validation and WAIC. *Stat. Comput.* 27:1413–1432. https://doi.org/10.1007/s11222-016-9696-4

Villani, A.C., R. Satija, G. Reynolds, S. Sarkizova, K. Shekhar, J. Fletcher, M. Griesbeck, A. Butler, S. Zheng, S. Lazo, et al. 2017. Single-cell RNA-seq reveals new types of human blood dendritic cells, monocytes, and progenitors. *Science*. 356:eaah4573. https://doi.org/10.1126/science.aah4573

Vukmanovic-Stejic, M., Y. Zhang, J.E. Cook, J.M. Fletcher, A. McQuaid, J.E. Masters, M.H. Rustin, L.S. Taams, P.C. Beverley, D.C. Macallan, and A.N. Akbar. 2006. Human CD4+ CD25hi Foxp3+ regulatory T cells are derived by rapid turnover of memory populations in vivo. *J. Clin. Invest.* 116:2423–2433. https://doi.org/10.1172/JCI28941

Wildenberg, M.E., C.G. van Helden-Meeuwsen, J.P. van de Merwe, H.A. Drexhage, and M.A. Versnel. 2008. Systemic increase in type I interferon activity in sjögren's syndrome: A putative role for plasmacytoid dendritic cells. *Eur. J. Immunol.* 38:2024–2033. https://doi.org/10.1002/eji.200738008

Zhang, Y., C. de Lara, A. Worth, A. Hegedus, K. Laamanen, P. Beverley, and D. Macallan. 2013. Accelerated in vivo proliferation of memory phenotype CD4+ T-cells in human HIV-1 infection irrespective of viral chemokine co-receptor tropism. *PLoS Pathog.* 9:e1003310. https://doi.org/10.1371/journal.ppat.1003310

JEM

Supplemental material

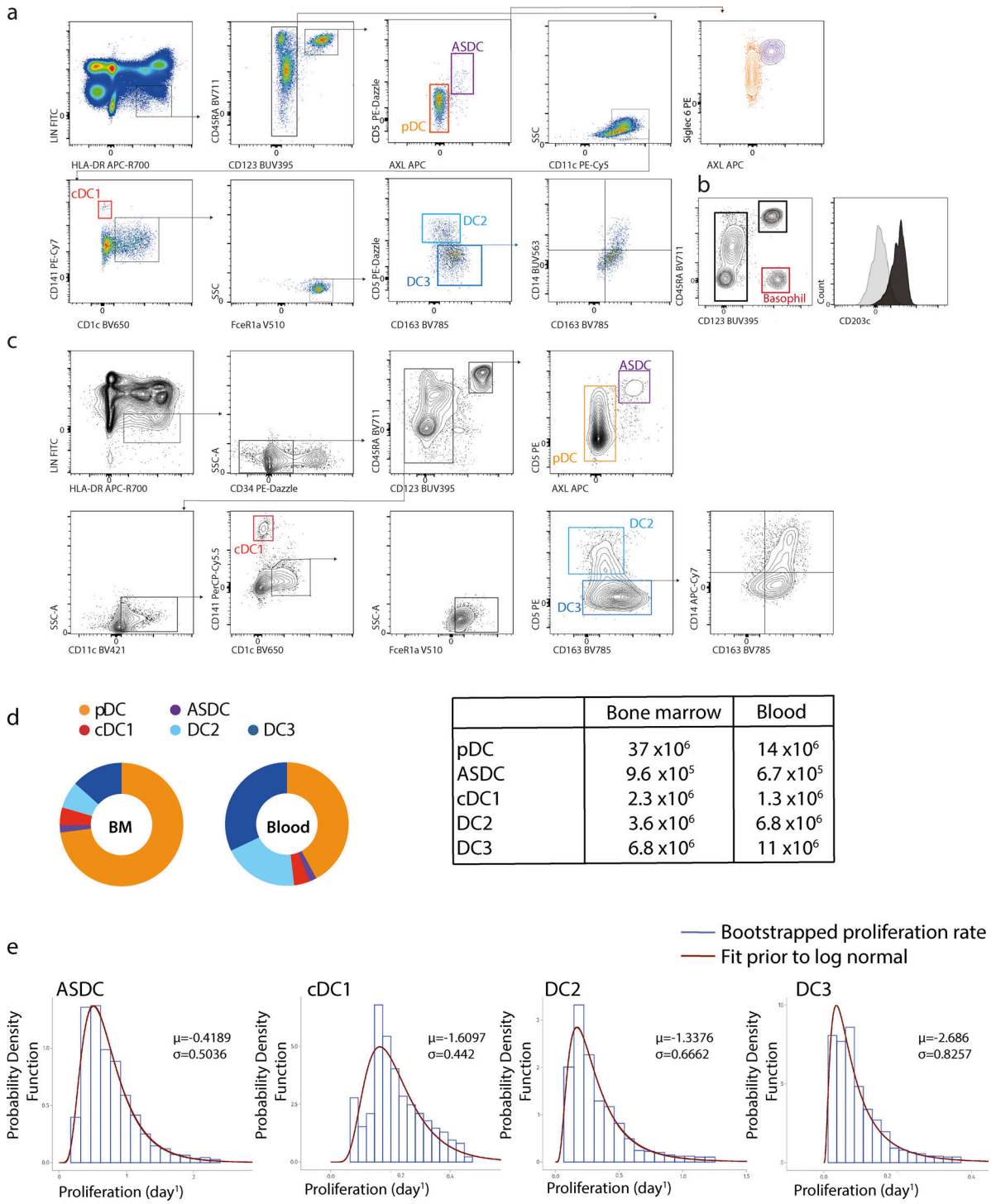

	Bone marrow	Blood
pDC	37×10^6	14×10^6
ASDC	9.6×10^5	6.7×10^5
cDC1	2.3×10^6	1.3×10^6
DC2	3.6×10^6	6.8×10^6
DC3	6.8×10^6	11×10^6

Figure S1. **Characterization of human DC subsets. (a)** Polychromatic flow cytometry gating strategy for blood DC subsets. Peripheral blood DC cells were identified as Lin⁻ HLA-DR⁺ cells. The DC subsets consist of pDC (CD123⁺ AXL⁻: orange gated population) and ASDC (CD123⁺ CD5⁺ AXL⁺ Siglec6⁺; purple gated population). cDC could be identified as CD123⁻ CD11c⁺ cells with cDC1 being CD141⁺ (red gated population), while cDC2 expressed CD1c⁺ FceR1a⁺ and was further divided into CD5⁺ DC2 and CD5⁻ DC3 (Cossarizza et al., 2021; Dutertre et al., 2019). **(b)** Polychromatic flow cytometry gating strategy for blood DC subsets sometimes identified a distinct HLA-DR⁺ Lin⁻ CD45RA⁻ CD123⁺ population (red square). Histogram below shows this population stained positive for the basophil marker CD203c (black) or FMO (grey). **(c)** Flow cytometry analysis of human DC subsets in the bone marrow. **(d)** Pie chart depicting the percentage of each DC population in the bone marrow and blood. The table shows the mean total DC in the blood and bone marrow, cells/person, from eight individuals. **(e)** The approximate daily proliferation rate was estimated for each population. The proliferation rate was defined as p = (fraction_SG2M/SG2M_length) * 24 h. Combining 10,000 bootstrap samples of the S/G2/M measurments (only including non-zero measurements) with samples drawn from a Uniform distribution (U[5, 15 h]), the approximate proliferation rate of all subsets was calculated. The prior distribution of a subset's proliferation rate was approximated by fitting a log-normal distribution to the bootstrap samples. The fitted parameters μ and σ, which are the mean and standard deviation of the samples' natural logarithm, respectively, are shown.

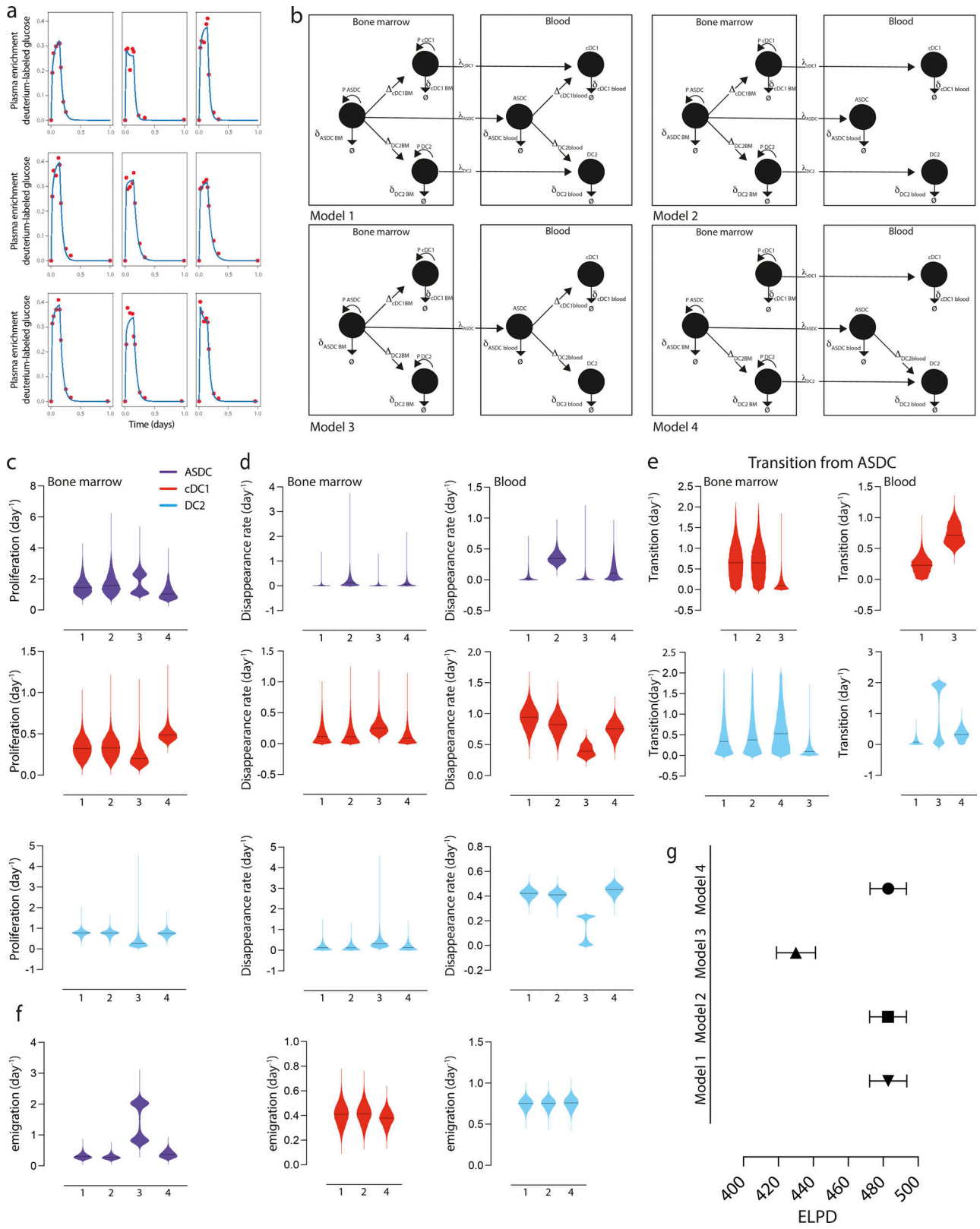

Figure S2. **Modeling human cDC kinetics. (a)** Deuterium-labeled glucose in the plasma of volunteers was measured before, during, and following the oral administration of 20 g deuterium-labeled glucose. **(b)** Potential models for circulating DC kinetics. The cartoon depicts four probable scenarios where ASDC develop into cDC1 and/or DC2. BM, bone marrow. **(c–f)** The parameters for (c) proliferation, (d) disappearance, (e) transition from ASDC, and (f) emigration for each model were quantified. **(g)** Model comparison. The out-of-sample predictiveness took the form of the elpd and their standard error was estimated via PSIS-LOO-CV for single data points for each model. Greater values indicate better relative predictive power of a model. Comparing the elpd values across models the elpd difference Δ elpd and the SD of the difference were calculated.

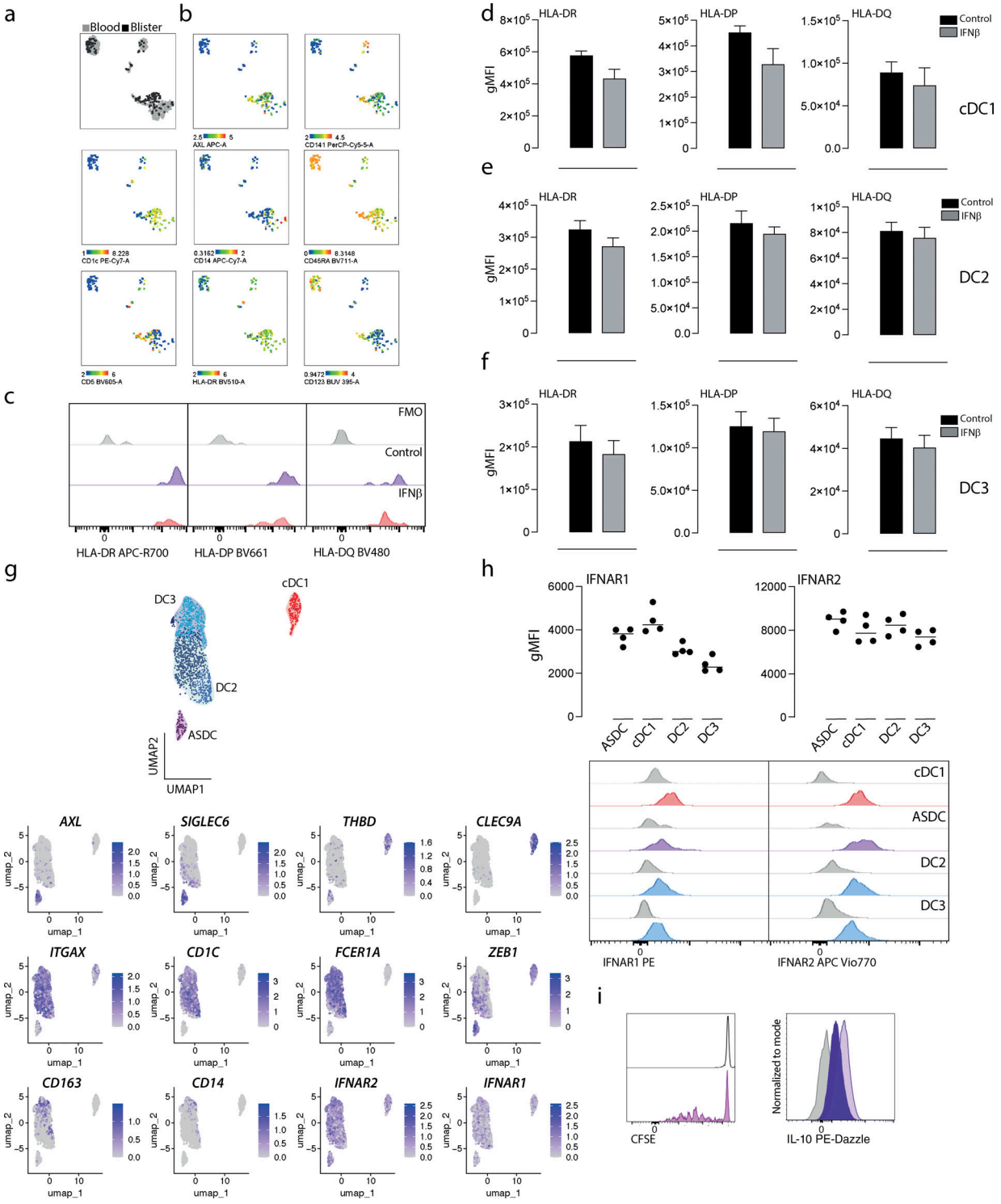

Figure S3. **Functional analysis of infiltrating ASDC. (a)** Infiltrating blister cells 24 h following an intradermal injection of 1.5 × 10^7 UV-killed *E. coli* into the forearm were index-sorted and analyzed by scRNAseq (Smart-seq2) from three individuals. scRNA-seq and protein expression data for each DC subset, using markers defined from FACS-indexed data from blister DC samples. These data was then integrated with blood DC data from Villani et al. and Dutertre et al. using the Seurat V3 pipeline (Dutertre et al., 2019; See et al., 2017; Villani et al., 2017). **(b)** Protein expression from FACS-indexed data of blister DC within the integrated UMAP space. **(c)** Representative flow cytometry histogram examining the effect of IFNβ on HLA expression on ASDC. **(d–f)** The expression of HLA-DR, -DP, or -DQ molecules was examined by flow cytometry following the incubation with either recombinant IFNβ or vehicle for 20 h on (d) cDC1, (e) DC2, and (f) DC3 subsets (n = 3–6 independent experiments performed in triplicate). **(g and h)** The expression of IFNAR1 or IFNAR2 was assessed in resting blood cDC populations using scRNA-seq and (h) flow cytometry (four individuals performed in triplicate). A representative flow cytometry histogram shows receptor expression (grey FMO). **(i)** Purified ASDC were either incubated with vehicle or IFNβ and then cultured with allogenic CFSE stained naïve T cells. Left: top, T cells alone, bottom with ASDC. Right: IL-10 expression on T cells after 7 days; grey FMO, dark purple with ASDC and vehicle pre-incubation, light purple ASDC with IFNβ pre-incubation.

Provided online are Table S1 and Table S2. Table S1 shows the list of DEGs used to identify each DC population. Table S2 compares ASDC between blood and blister.